

5.0 GLOBAL AXISYMMETRIC ANALYSIS

5.1 Overview of Pretest Model

The pretest axisymmetric model represents the 135 degree azimuth, which was assumed to be typical of a "free-field" azimuth, away from buttresses or penetrations. Figure 5-1 illustrates the model. The ABAQUS [5] general purpose finite element program Version 5.8-15, along with the ANACAP-U [4] concrete and steel constitutive modeling program, were used for all pretest analyses [1]. Tendons and their prestressing were modeled to replicate expected tendon stress-strain behavior and friction effects; however, axisymmetric modeling does not allow tendon slip modeling for the hoop tendons, only for the vertical tendons. The pretest axisymmetric grid had 12 elements through the wall thickness near the basemat. The concrete and liner were represented with 8-node quadrilateral elements (ABAQUS CAX8R) and 3-node axisymmetric shell elements, respectively. The total number of elements used was 2009.

The reinforcement in the structure was represented with ABAQUS rebar subelements. These subelement stiffnesses are overlaid onto the parent concrete elements in which they reside, but do not have separate degrees of freedom, and so have strain compatibility with the concrete. The rebar stress-strain behavior is evaluated separately from the concrete, however. The bottom of the model was supported by nonlinear contact springs, with "zero" resistance to uplift and very high compression stiffness. The subgrade stiffness was not considered.

One complex aspect of the pretest analysis models (both global and local) was the tendon modeling. Significant effort was exercised in the tendon representation in order to:

1. Calculate the tendon stress distribution throughout the pressurization sequence, including the effects of friction;
2. Calculate the displacements of the concrete wall correctly, since this drives the liner, thereby driving the prediction of liner strain concentrations.

The vertical tendons were modeled with 144 truss elements (with friction ties to adjacent concrete nodes) and 36 axisymmetric shell elements. Axisymmetric shells were used in the dome to represent the smeared hoop and vertical components of the hairpin tendons. This avoided the mathematical difficulty of terminating tendon elements at the dome apex with a finite cross-section area but zero radius. Hoop tendons were modeled as rebars, so they were always bonded to the concrete. The model was prestressed with the ABAQUS *INITIAL STRESS command in conjunction with the *PRESTRESS HOLD option (for the hoop tendons) that allowed the model stresses to equilibrate, while forcing the hoop tendon stresses to remain at predetermined levels.

Pressure load was applied to all interior model surfaces over 161 increments. The ABAQUS feature DIRECT=NOSTOP was used with five iterations per load step. The five iterations ensure that materials in the plastic range stay on a yield surface, but the "NOSTOP" parameter allows advancement of the solution before achieving full force convergence, which is difficult to achieve in cracked concrete elements. Instead of achieving force convergence, the displacement convergence at each increment was monitored to ensure the quality of the solution.

Some results of the axisymmetric analysis are plotted in Figures 5-2, 5-3, and 5-4. As in Chapter 4, results of both the 1999 (pretest round-robin submittal) and the 2000 pretest analysis are plotted. The primary difference in the two analyses is the vertical tendon prestressing—the 2000 analysis introduces large friction losses into the straight run of vertical tendon. These figures show displacements versus pressure at several points on the model. The vertical grid lines on the pressure history plots represent multiples of design pressure, $P_d = 0.39$ MPa. A comparison of these results to the test were provided in Chapter 4. For radial response, different critical milestones can also be noted by the changes in curve slope. Cylinder cracking coincides with the slope jump in the curves at about 1.7 P_d . Progressive yielding of steel elements corresponds to the gradually increasing slope of the displacement curves.

The two primary damage locations predicted by the axisymmetric analyses were the cylinder midheight and the wall-basemat juncture. The largest strains tended to occur near the inner corner of the wall-basemat juncture, in the concrete near the liner anchor embedment. The pretest study of potential shear failure at the wall-basemat juncture showed that while wall-basemat outer surface concrete crushing (compressive stress reaching f_c') was predicted to occur by 3.2 P_d , a through-wall shear failure was not likely until at least 4.0 P_d . Other failure modes were judged to be more likely prior to reaching this pressure. This prediction appears to have been borne out by the test. Note that, although no evidence

of “crushing” was observed on the outside surface of the cylinder wall-base, f_c' may have been reached as predicted by analysis. Visible evidence of crushing would only occur at compressive strains that are much larger than the -0.0025 required to reach stress of f_c' . Strains of about 0.005 would be necessary for visible spalling to occur.

5.2 Changes to Pretest Model

While the predicted radial expansion behavior of the cylinder was accurate (within ~4%) with the pretest model, as outlined in Chapter 4, the basemat uplift and dome vertical displacement were significantly overpredicted. A posttest analysis effort was undertaken by making changes to the axisymmetric model to calibrate to the test. Initially, the following changes were made strictly to assess the sensitivity to these changes:

1. 10% additional prestress was added to the vertical tendons,
2. 10% additional vertical prestress area was added to the dome, and
3. Very thorough check of basemat rebar input was conducted.

Initial posttest analyses were run with ABAQUS Version 5.8-15. Results of these initial sensitivity analyses for vertical tendon prestress showed some promise in getting closer to the test measurements. However, early in 2001, the authors started using ABAQUS Version 5.8-18 in an effort to ensure that all of the PCCV analysis work would be upwardly transportable to new versions of ABAQUS. When this version transfer was made, a significant program bug was found in 5.8-18 (and 5.8-21) related to the use of prestress hold and small deflection theory. (Note that small deflection theory was used in conjunction with the tendon friction modeling strategy adopted for the curved portions of tendons.) This bug was finally resolved by ceasing to use the prestress hold option. Currently, Version 5.8-18 for all analyses is used, but without prestress hold, by increasing the prestress by trial and error to account for elastic shortening. Confirmation that the new strategy and new version can now replicate the pretest results is provided in Figures 5-2, 5-3, and 5-4. This is a significant finding and change in solution strategy for the conduct of containment analysis using ABAQUS.

Once this bug was resolved, global model calibration was continued and consisted of the following steps.

1. Basemat rebar checking was completed, and checked out ok.
2. A basemat spring sensitivity study was conducted.

The basemat spring study began by a two order of magnitude softening of the support spring compression stiffness. This produced very little change in results. Then a hand calculation of the supporting soil stiffness (as transmitted through the mudmat) was performed and incorporated into the model. The weight of the PCCV model (including the instrumentation frame) was calculated to be approximately

$$W = 4,800 \text{ kips.}$$

A stiffness along the bottom of the basemat was assumed based on a total dead load deflection of 0.1 inch (2.5 mm). This is based on an assumption of typical subgrade properties working in conjunction with the 15-cm-thick concrete mudmat. Then the basemat spring stiffnesses were distributed based on tributary area following the 1/6:2/3:1/6 rule for isoparametric elements with mid-side nodes. This produced vertical uplift displacements that were less than the pretest analysis, but still much larger than the test measurements. As a sensitivity check, one order of magnitude softening and stiffening of the compressive springs was introduced and analyzed. The results of the basemat compression spring sensitivity evaluation are summarized below.

- Pretest solution was based on an "essentially" rigid base with zero tensile resistance.
- Adjusting the *distribution* of forces on the underside of the basemat by assigning stiffness according to tributary areas achieved minor reduction in uplift and more rational distribution of support forces, but the compression stiffness assumed was still very stiff. This means that even small basemat flexure or bulging is manifested as uplift, i.e., the bulging is reacted against a rigid surface.

- Trying softer stiffnesses to account for soil behavior tends to increase basemat flexure, but this is compensated by the “starting point” of uplift, i.e., the negative displacement due to dead load before pressurization. The results of the foundation stiffness sensitivity cases are plotted in Figures 5-5, 5-6, and 5-7.

Through this foundation sensitivity study, insights have emerged that, in the authors’ opinion, explain the basemat displacement phenomena and why the basemat uplift measurements showed essentially zero uplift. The basemat underside pressure for the final two axisymmetric analyses are plotted in Figures 5-8 and 5-9, and a deformed shape for the final posttest case is plotted in Figure 5-10. With the refined foundation spring modeling, the absolute (without rezeroing or adjusting for dead load) displacements of the center of the basemat and the outer edge of the basemat are plotted in Figure 5-11. This shows that under deadload, the basemat settles downward roughly uniformly by about -2.54 mm. This is a direct result of the foundation stiffness assignment based on engineering judgment. During pressurization, however, the center and edge displace very differently. As the basemat flexes, the contact pattern shrinks (as shown in Figures 5-8 to 5-10) so the weight of the model is distributed over a smaller area and settles deeper into the soil (i.e., more downward displacement occurs). At the edge, however, the displacement begins rising until finally, at about 2.5 Pd, it becomes positive. It is reasonable to assume (as drawn in Figure 5-10) that the mudmat, which is several orders of magnitude more flexible than the basemat, will follow the dished shape of the basemat. All parts of the mudmat are likely to elastically rebound as bottom surface pressures decrease at the outer radii. This elastic rebounding will continue until the absolute displacement crosses zero, the point where the soil was stress-free prior to constructing the model. This theory explains how, even with some appreciable basemat flexure, the mudmat could remain in contact with the basemat at relatively high pressures, and thus register virtually zero displacement measurement. Late in the LST, the outer edge of the basemat might have begun to uplift slightly, but without detailed soil stiffness measurements this would be very difficult to predict. It is even possible that the outer edge of the mudmat could have lifted slightly simply due to kinematics (as shown in Figure 5-10), but this too was impossible to measure. Note that all of the displacements associated with this basemat flexure phenomenon are very small (~ 2 mm).

The final foundation stiffnesses used in the posttest analysis were judged reasonable, forming the basis of the final axisymmetric analyses. In the revised comparison to SOL #1, the analysis result was plotted as zero when the result was negative, and positive when it crossed the axis. Per the preceding discussion, this result represents the stress/force neutral point of the supporting soil prior to constructing the model and the point after which the mudmat might stop following the underside of the basemat.

The last set of modeling changes dealt with the dome. In the final posttest analysis, the stressing of the vertical tendons was kept the same as in the 1999 analysis (no friction along the straight portion) because it agreed best with measured and observed behavior. The dome tendon strategy, however, was modified. The change was based on the observation that the nonaxisymmetric geometry of the “hairpin” tendons, at azimuths such as 135 degrees, leads to contributions from both sets of hairpin tendons. Both sets intersect the 135-degree r-z plane at 45 degrees. Thus it was deduced that the effective thickness for the shell used to model the vertical tendons is actually $2\cos(45 \text{ degrees})$ times the thickness used in the pretest analysis. The final posttest analyses reflect this change, i.e., a 41% increase in dome tendon area, which provided improved correlation to the test.

5.3 Results and Comparisons

The displacement profiles at the 135 degree azimuth that were compared to the pretest analysis are recompared to the final posttest analysis in Figure 5-12. All of the axisymmetric analysis results are then recompared to the test in Figures 5-13 through 5-23. The LST converted and temperature corrected data is plotted along with a posttest analysis using the 1999 model with modified basemat “soil” springs, added dome tendon thickness, and a set of curves labeled “Final Posttest.” The final posttest analysis is the same as the “1999-Soil-Mod-5-Dome,” but with updated material properties to match those used immediately prior to the test. Both curves are provided for comparison. For most of the data locations, the most up-to-date material properties provide the closest correlation. This is especially true of the radial displacement plots, SOLs 2 through 6.

All of the wall-base juncture comparisons are replotted with the final posttest analysis in Figures 5-24 through 5-46.

The plots and discussion in this section provide an explanation of basemat uplift behavior, and dome vertical displacement correlation is improved, but is still overpredicted by analysis. Prediction of radial displacement at the springline (SOL 7) is also low by about a factor of 2, but all other behavior comparisons show generally good correlation.

5.4 Conclusions on Global Analysis

The conclusions reached about the global axisymmetric analyses performed for the project and discussed in Chapter 4 and 5 are summarized below.

- Pretest Analysis: Radial displacements were generally well predicted by global axisymmetric analysis, but dome and vertical displacements were significantly overpredicted.
- Posttest Analysis: uplift and displacement predictions were significantly improved by softening and redistributing soil basemat springs according to tributary area. Dome displacements were improved by thickening the dome meridional tendon representation due to the rectilinear hairpin layout.
- The behavior predictions were improved by using no vertical tendon friction in the cylinder.
- Wall-base juncture behavior was well predicted by the detailed wall-base juncture (axisymmetric) modeling, and by the pretest analysis, but was further improved in the final posttest analysis.
- Analysis with the 5.8 series versions of ABAQUS should not use the prestress hold option. In general, a trial-and-error method for choosing prestress levels that equilibrate to the desired levels has proven reliable.

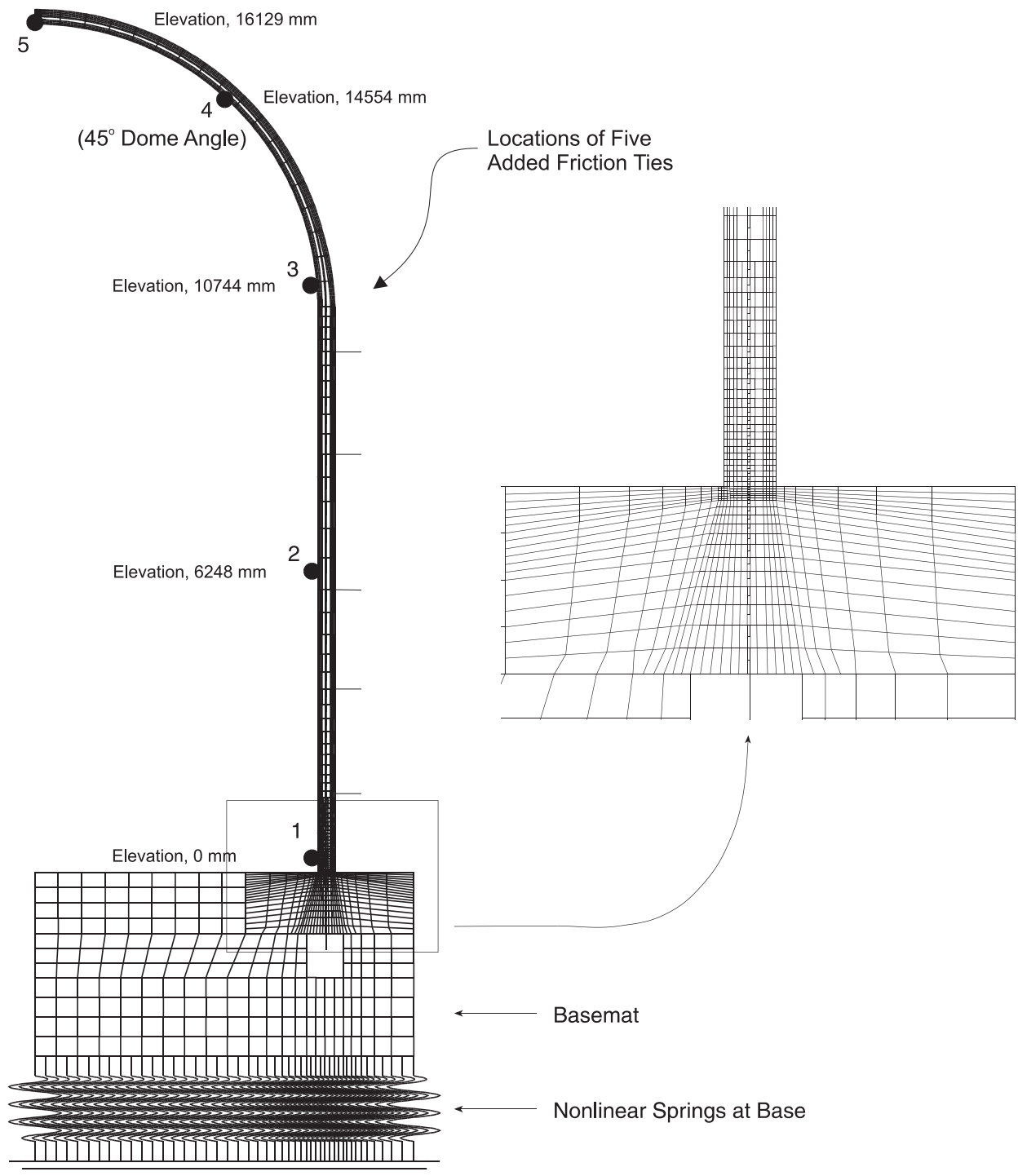
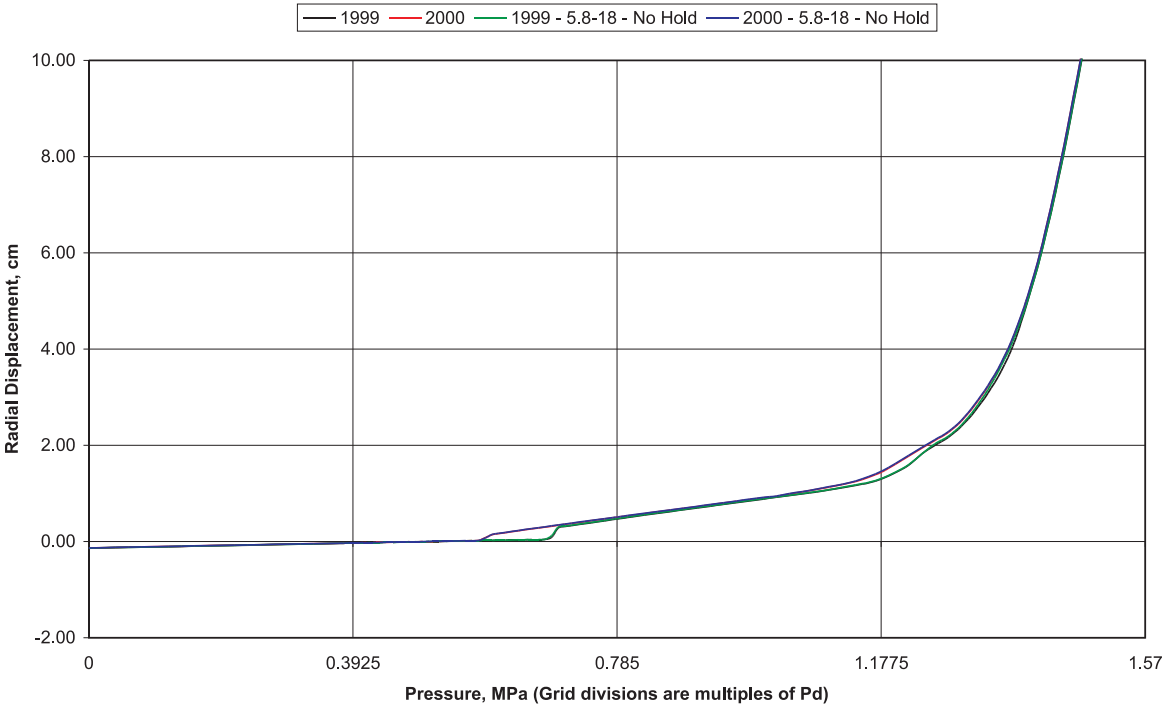


Figure 5-1. Axisymmetric Model of PCCV and Locations for Plotted Output

**Axisymmetric Analysis with Modified Spring Stiffness
Radial Displacement as a Function of Pressure - Elevation: 6248 mm**



**Axisymmetric Analysis with Modified Spring Stiffness
Radial Displacement as a Function of Pressure - Elevation: 10744 mm**

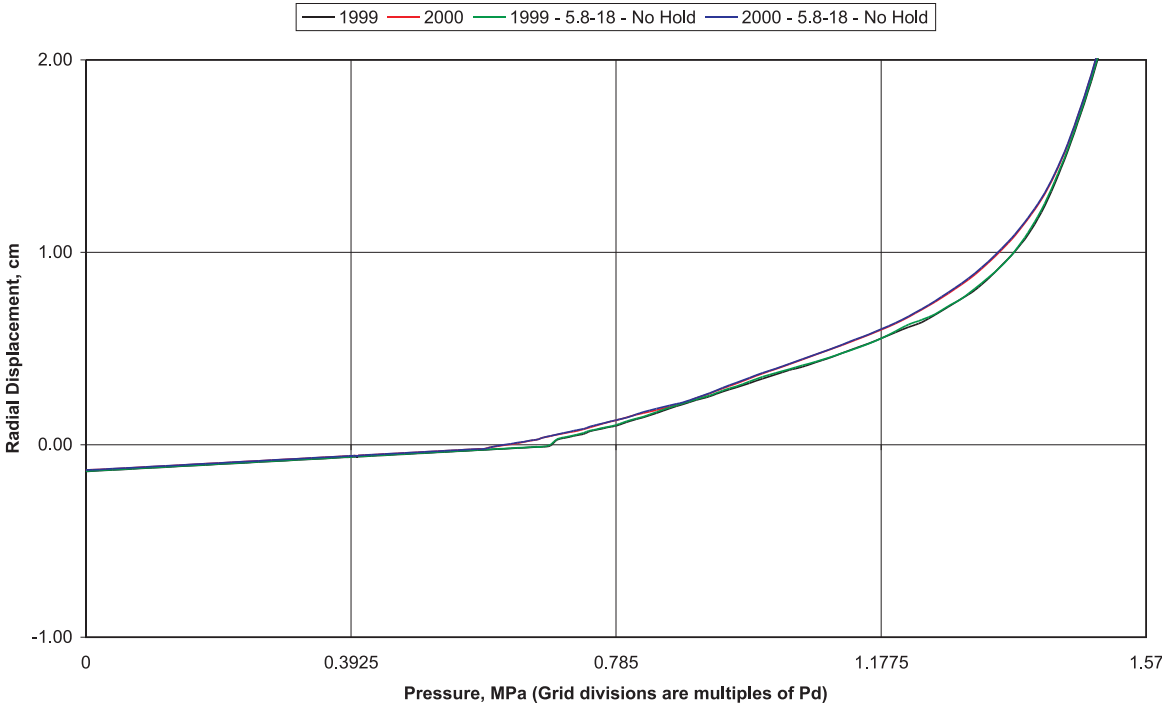
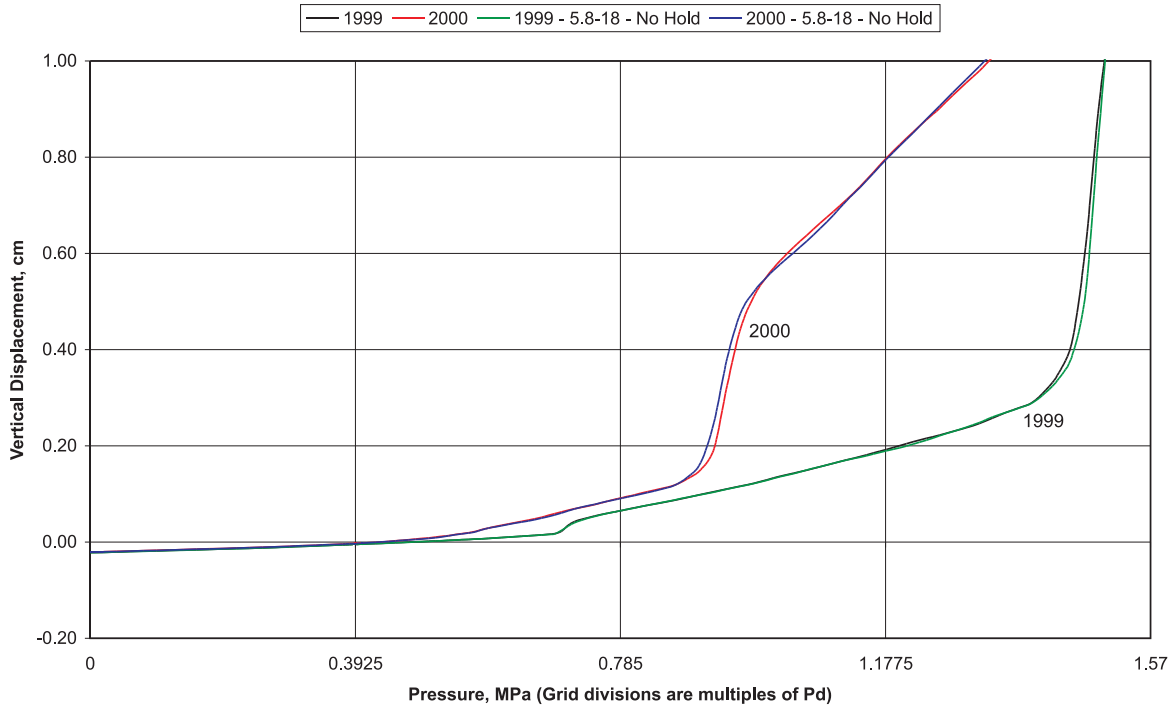


Figure 5-2. Radial Displacements Comparison of Pretest and Posttest Analysis using Different ABAQUS Versions and No Prestress Hold

**Axisymmetric Analysis with Modified Spring Stiffness
Vertical Displacement as a Function of Pressure - Elevation: 0 mm**



**Axisymmetric Analysis with Modified Spring Stiffness
Vertical Displacement as a Function of Pressure - Elevation: 10744 mm**

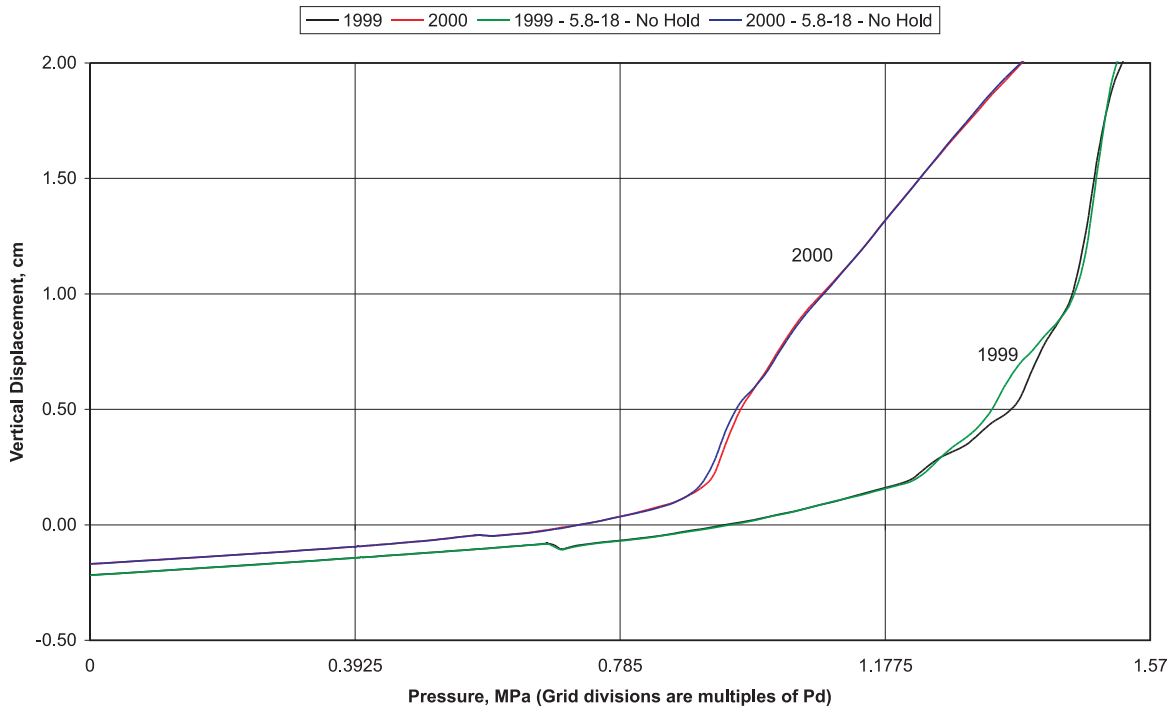
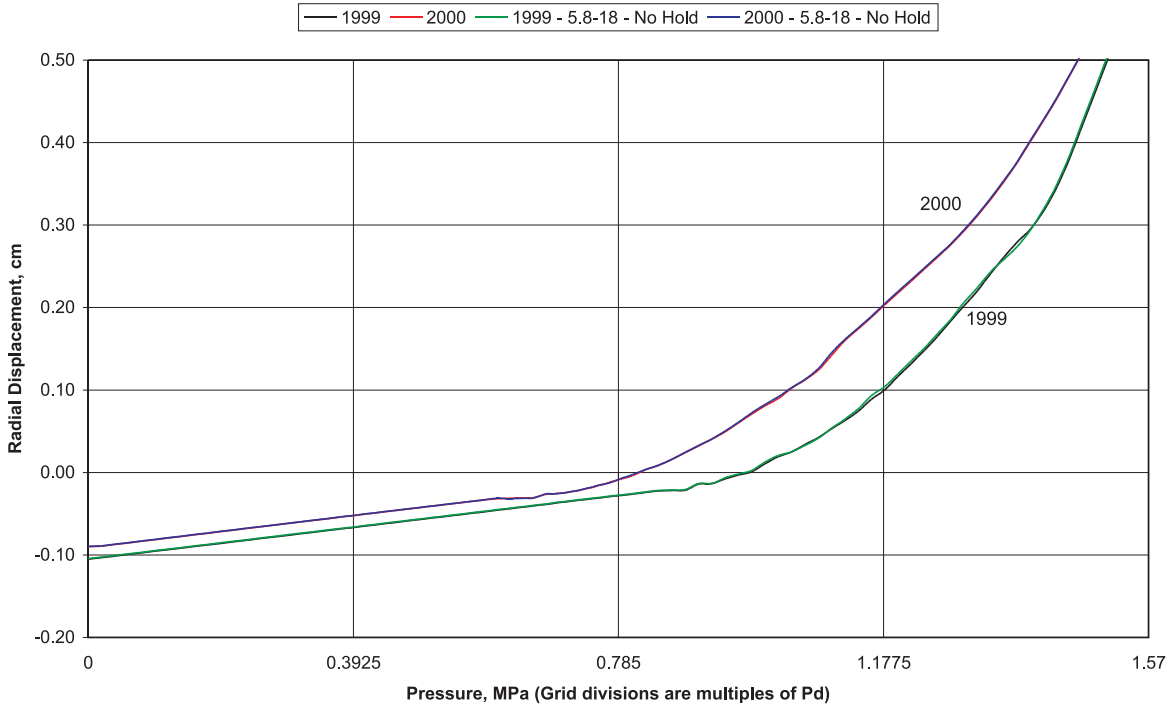


Figure 5-3. Vertical Displacements Comparison of Pretest and Posttest Analysis using Different ABAQUS Versions and No Prestress Hold

**Axisymmetric Analysis with Modified Spring Stiffness
Radial Displacement as a Function of Pressure - Elevation: 14554 mm**



**Axisymmetric Analysis with Modified Spring Stiffness
Vertical Displacement as a Function of Pressure - Elevation: 16129 mm**

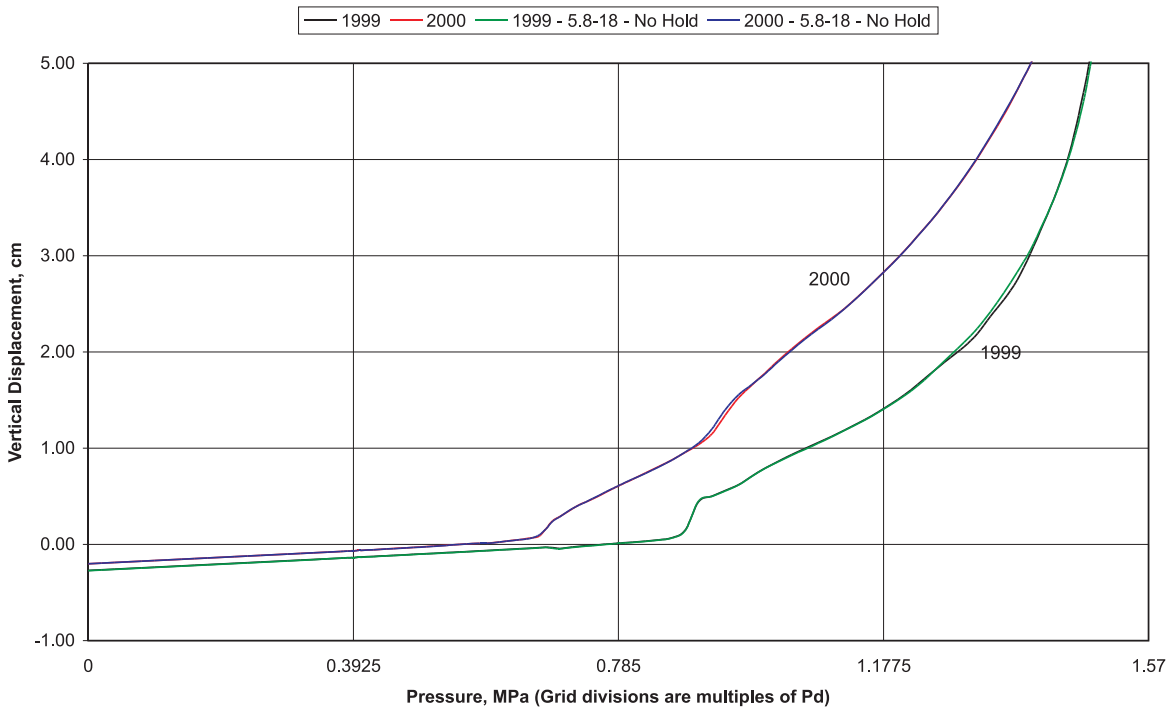
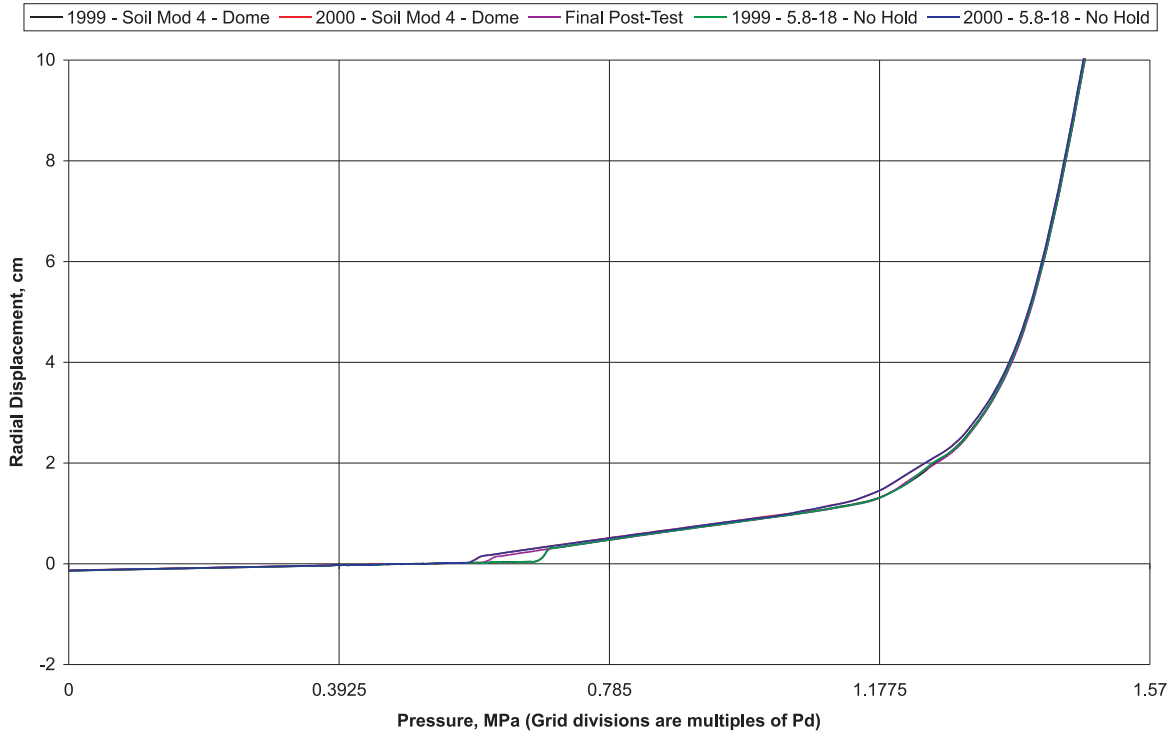


Figure 5-4. Dome Displacements Comparison of Pretest and Posttest Analysis using Different ABAQUS Versions and No Prestress Hold

Axisymmetric Analysis, Radial Displacement as a Function of Pressure - Elevation: 6248 mm



Axisymmetric Analysis, Radial Displacement as a Function of Pressure - Elevation: 10744 mm

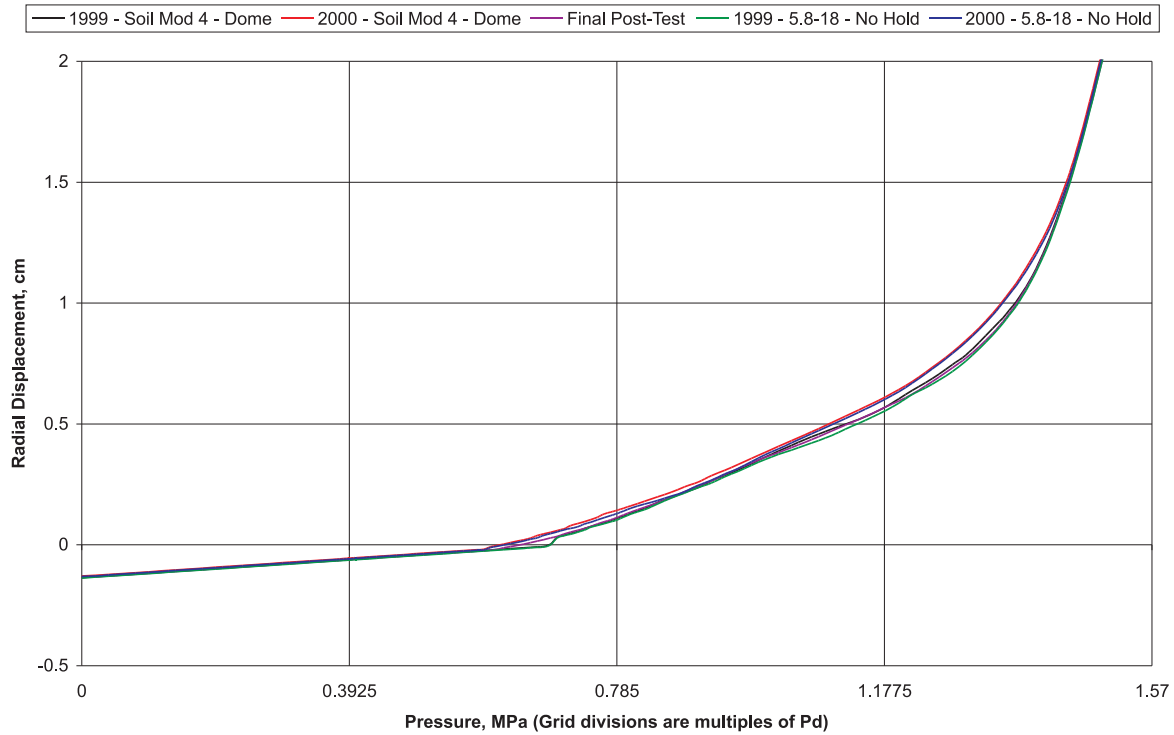
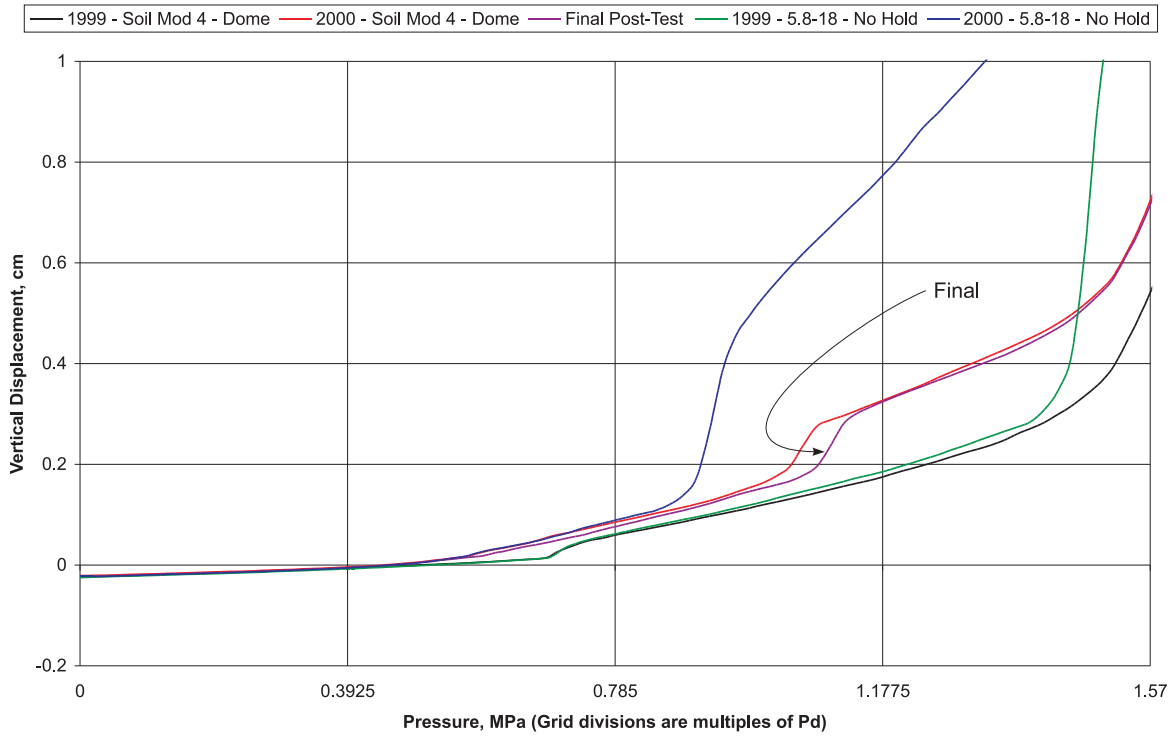


Figure 5-5. Radial Displacements Comparison of Pretest and Posttest Analysis using Different ABAQUS Versions and No Prestress Hold

Axisymmetric Analysis, Vertical Displacement as a Function of Pressure - Elevation: 0 mm1



Axisymmetric Analysis, Vertical Displacement as a Function of Pressure - Elevation: 10744 mm

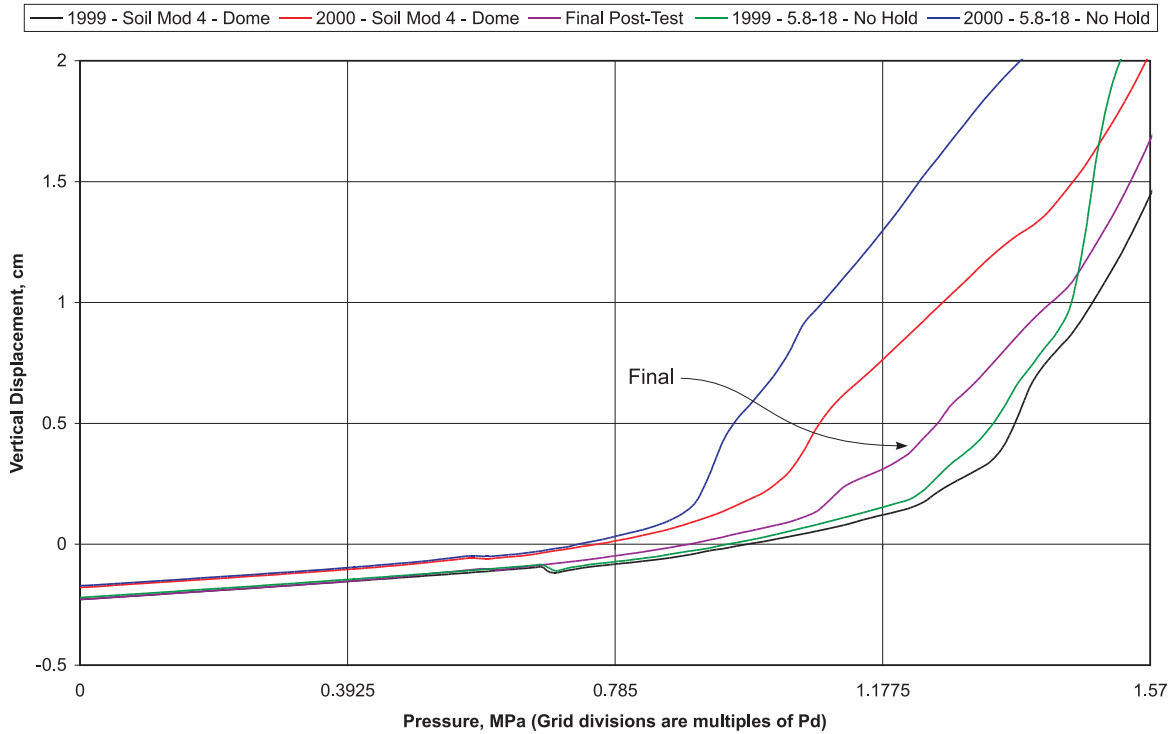
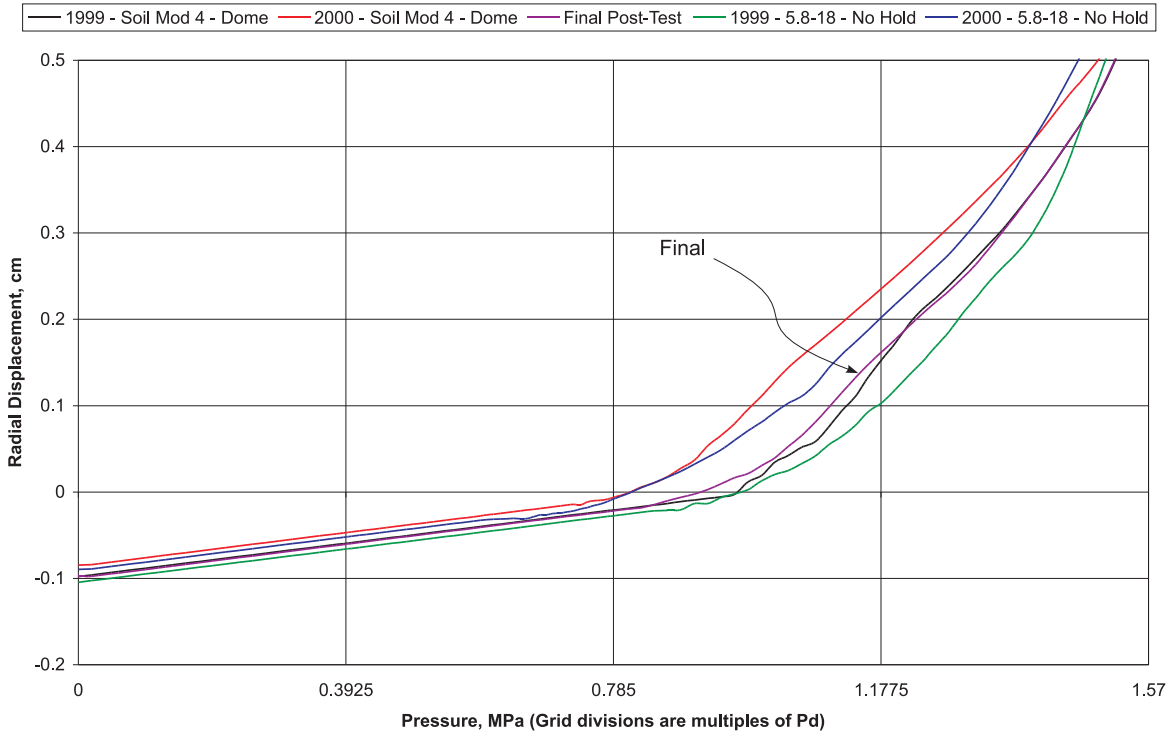


Figure 5-6. Vertical Displacements Comparison of Pretest and Posttest Analysis using Different ABAQUS Versions and No Prestress Hold

Axisymmetric Analysis, Radial Displacement as a Function of Pressure - Elevation 14554 mm



Axisymmetric Analysis, Vertical Displacement as a Function of Pressure - Elevation: 16129 mm

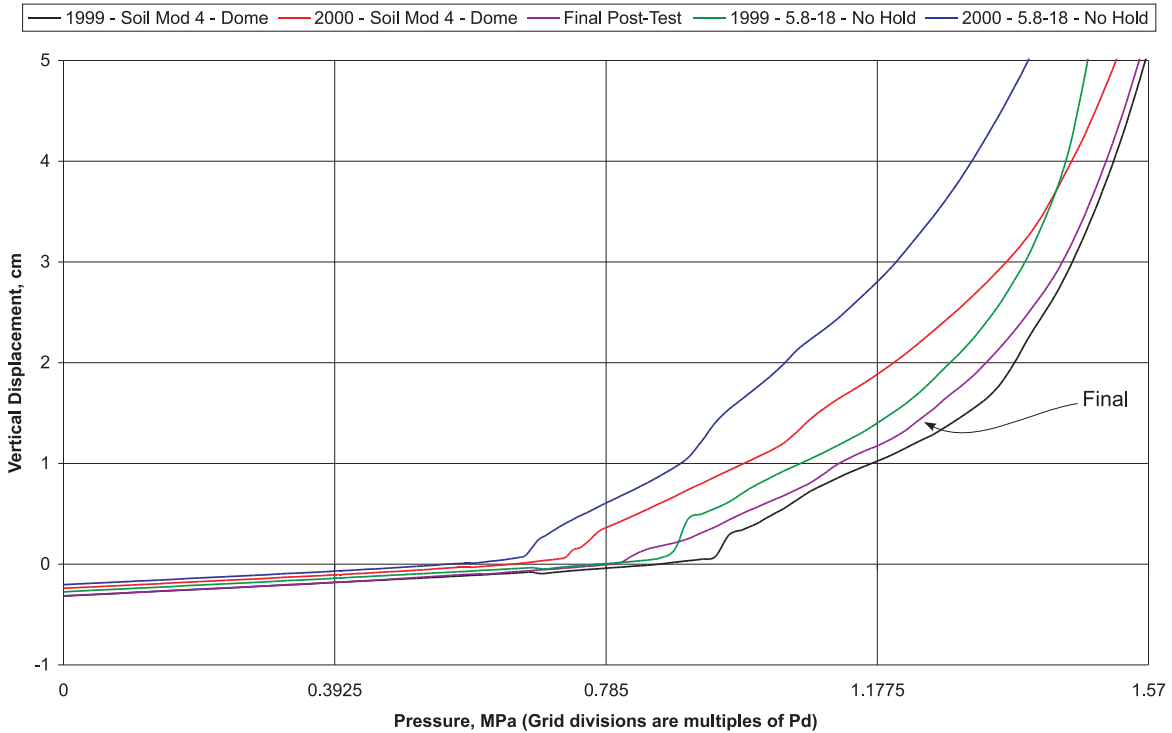


Figure 5-7. Dome Displacements Comparison of Pretest and Posttest Analysis using Different ABAQUS Versions and No Prestress Hold

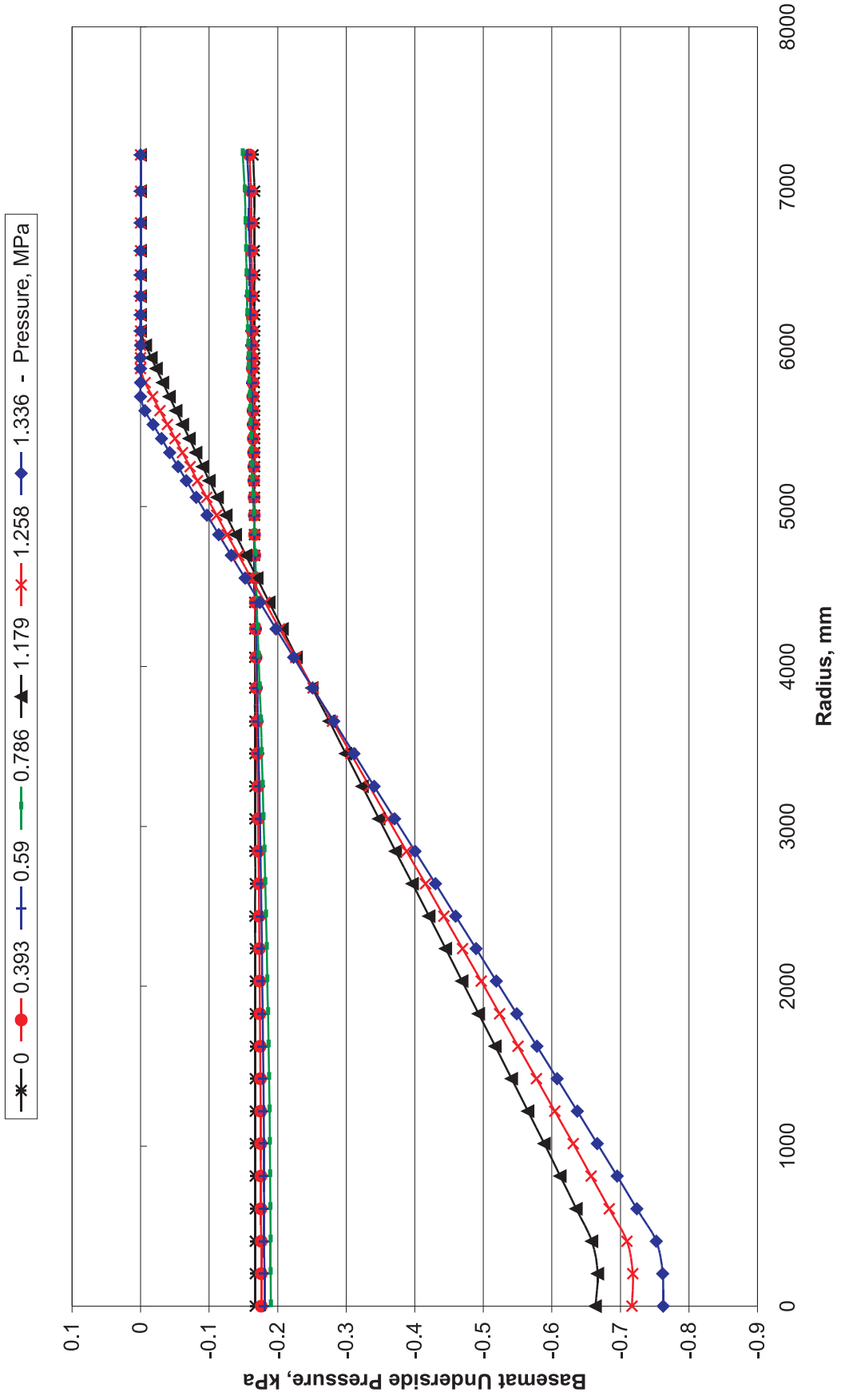


Figure 5-8. Basemat Underside Pressure versus Radius, 1999 Analysis with Final Soil Springs and Dome

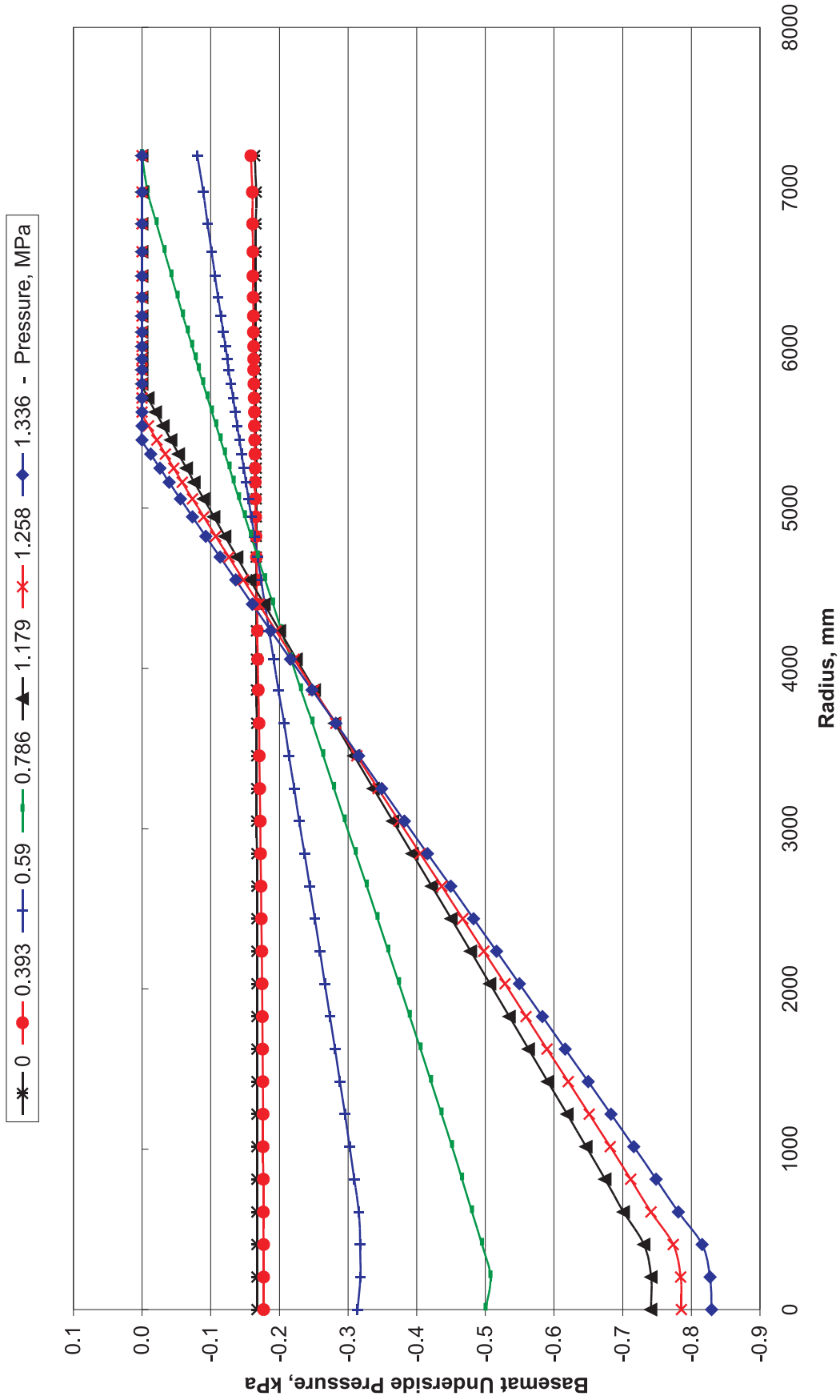


Figure 5-9. Basemat Underside Pressure versus Radius, 2000 Analysis with Final Soil Springs and Dome, and No Straight Tendon Friction

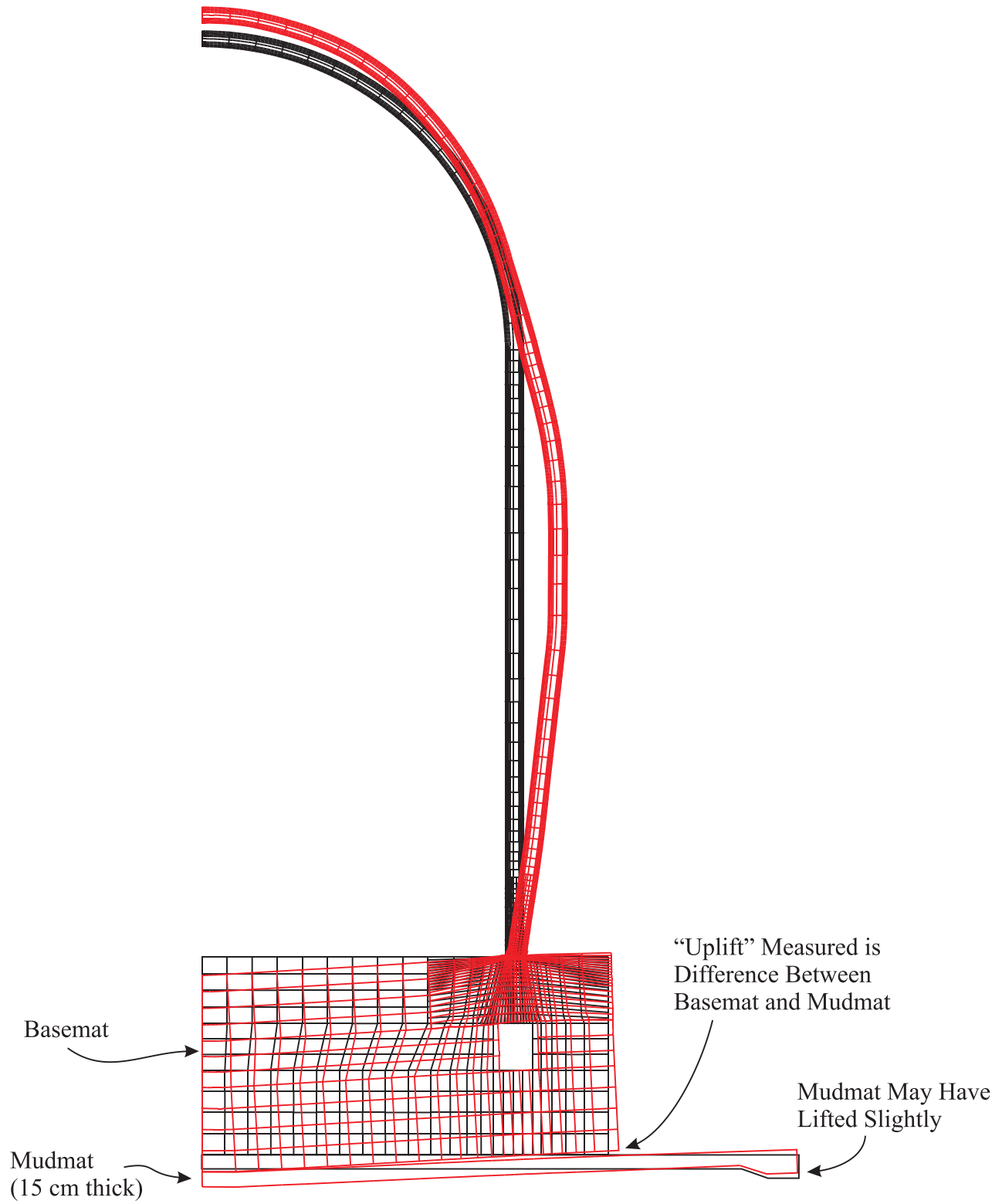


Figure 5-10. Illustration of Basemat/Mudmat Uplift

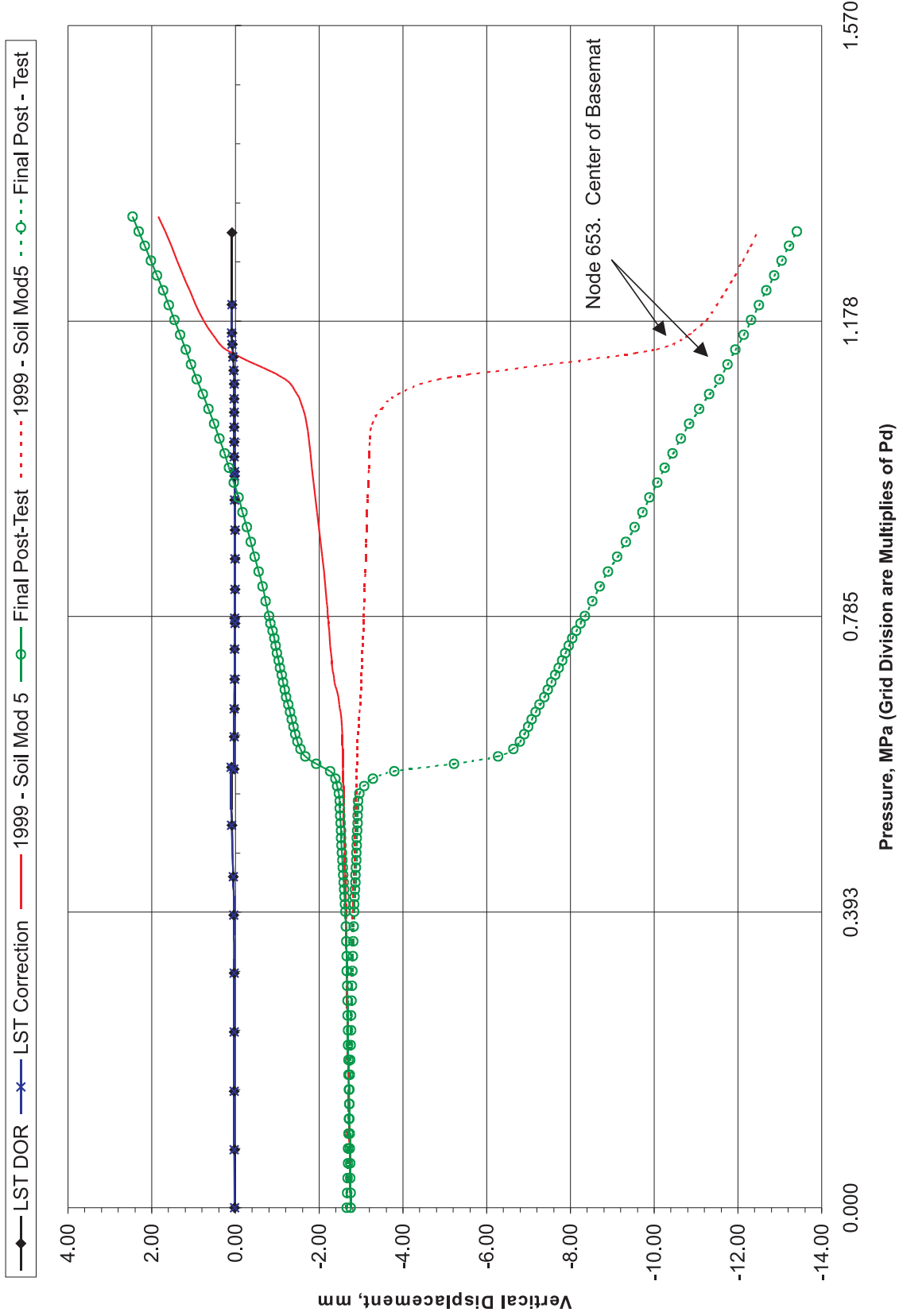


Figure 5-11. Standard Output Location #1. Azimuth: 135 Degrees, Elevation: 0.00 Meters, Top of Basemat

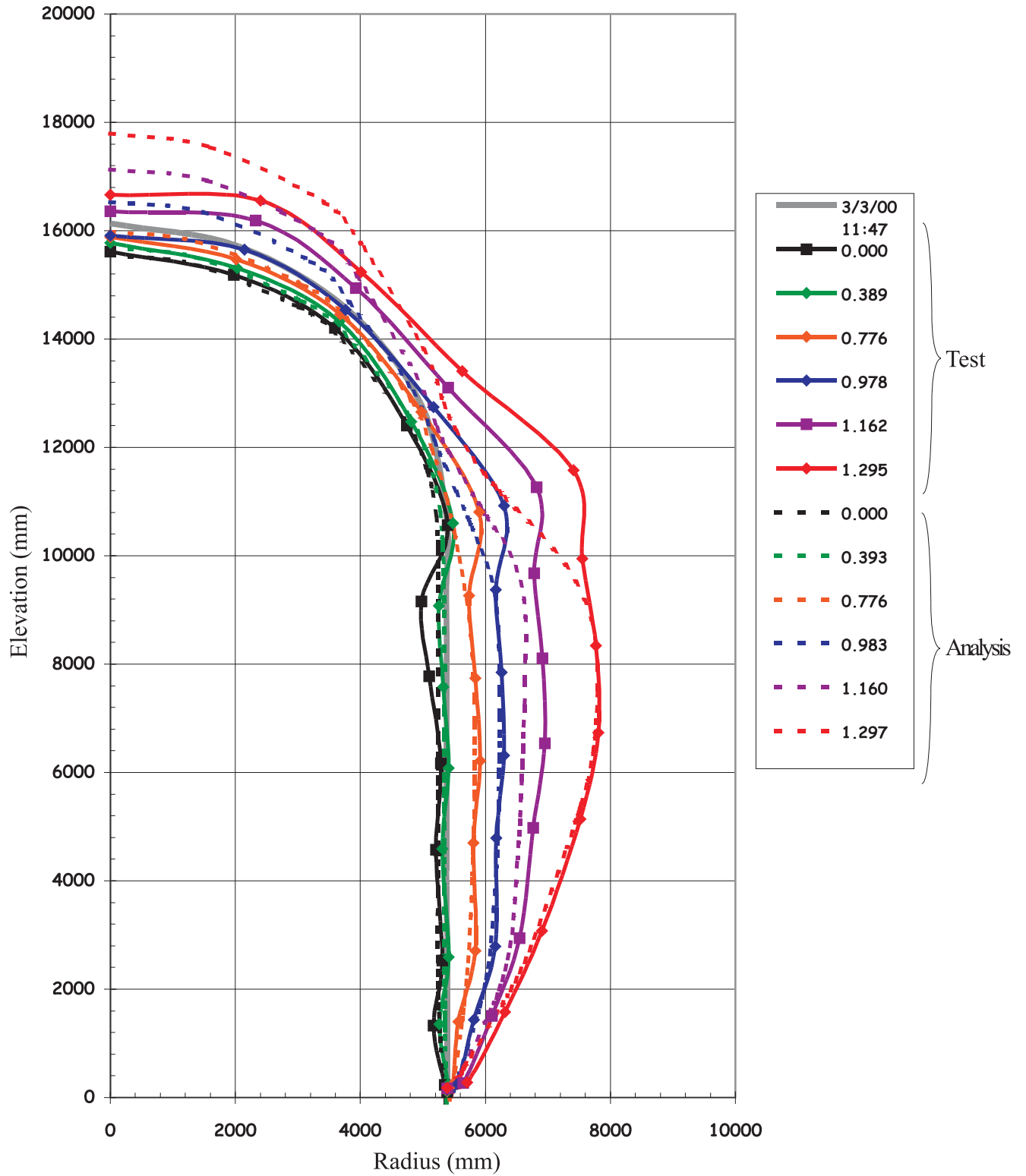
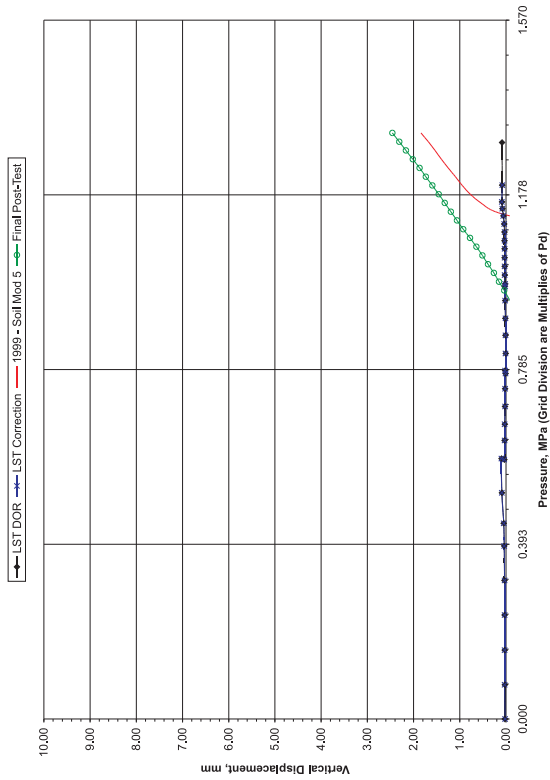
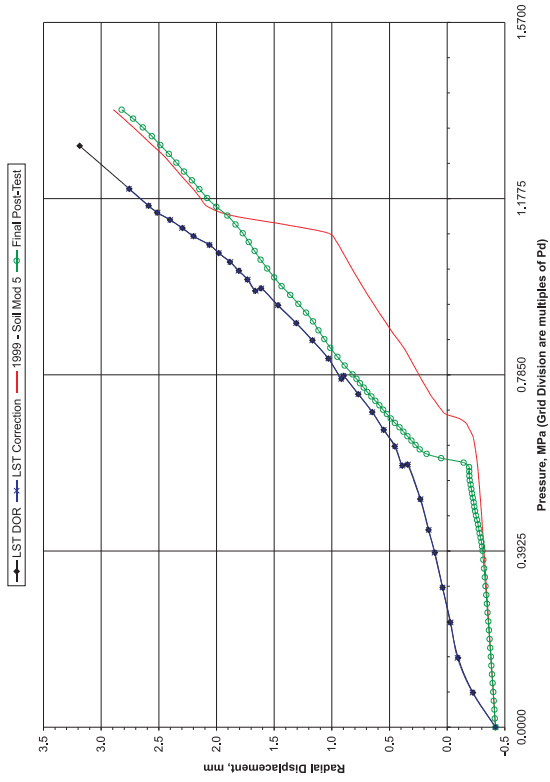


Figure 5-12. PCCV LST - Deformation @ Azimuth 135 (Z) × 100 Compared to Axisymmetric Final Posttest Analysis

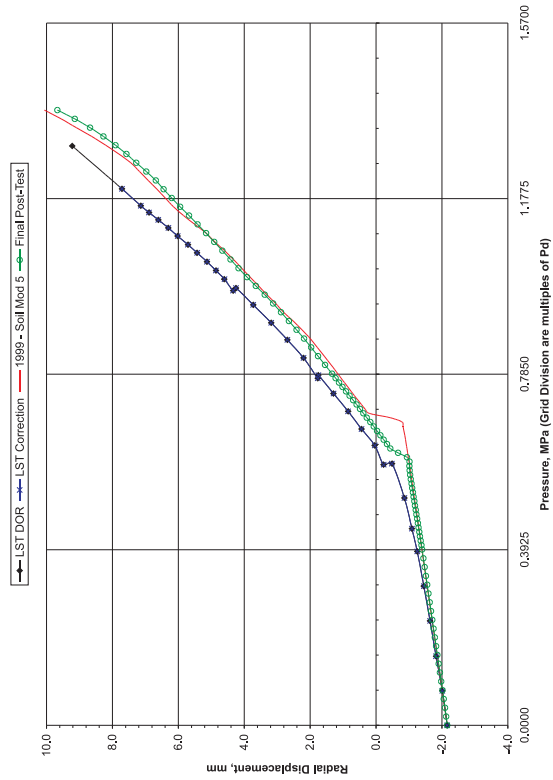
Standard Output Location #1. Azimuth: 135 Degrees, Elevation: 0.00 Meters, Top of Basemat



Standard Output Location #2. Azimuth: 135 Degrees, Elevation: 0.25 Meters, Base of Cylinder



Standard Output Location #3. Azimuth: 135 Degrees, Elevation: 1.43 Meters, Base of Cylinder



Standard Output Location #4. Azimuth: 135 Degrees, Elevation: 2.63 Meters, Base of Cylinder

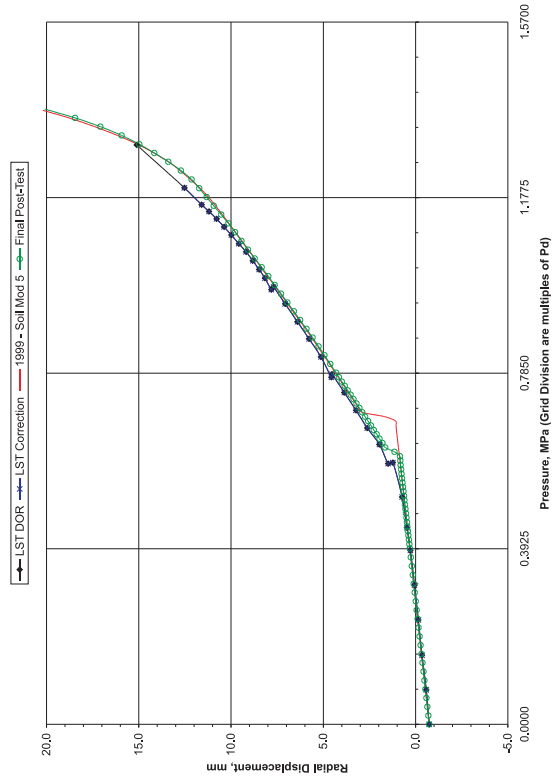
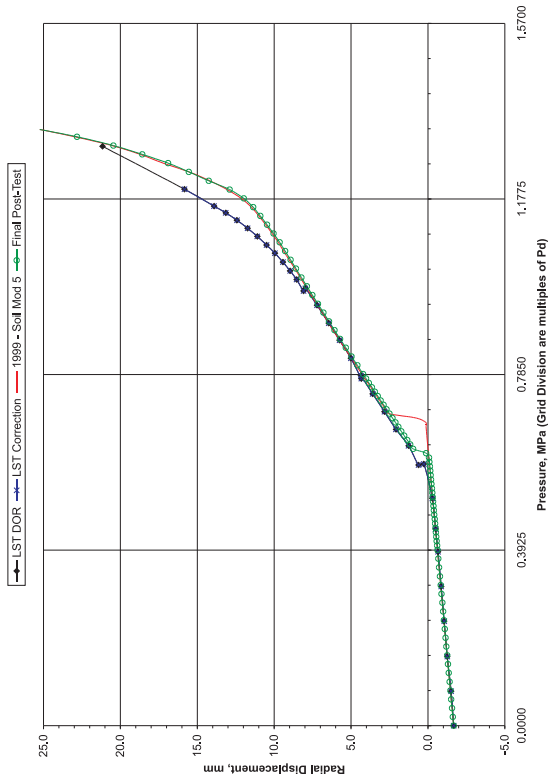
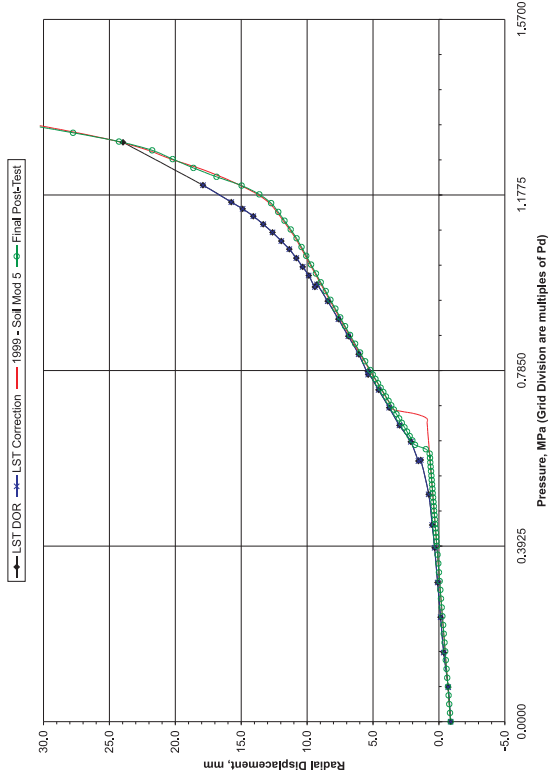


Figure 5-13. Comparisons at Standard Output Location 1, 2, 3, and 4

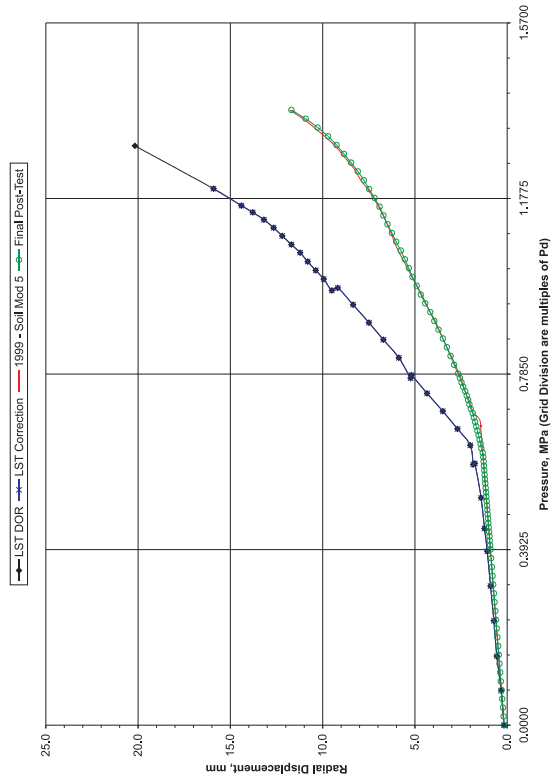
Standard Output Location #5. Azimuth: 135 Degrees, Elevation: 4.68 Meters, EH Elevation



Standard Output Location #6. Azimuth: 135 Degrees, Elevation: 6.20 Meters, Approximate Midheight



Standard Output Location #7. Azimuth: 135 Degrees, Elevation: 10.75 Meters, Springline



Standard Output Location #8. Azimuth: 135 Degrees, Elevation: 10.75 Meters, Springline

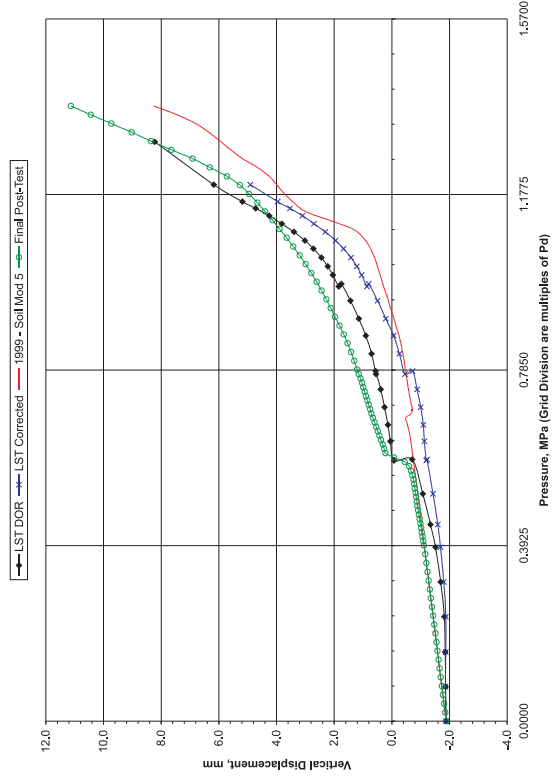
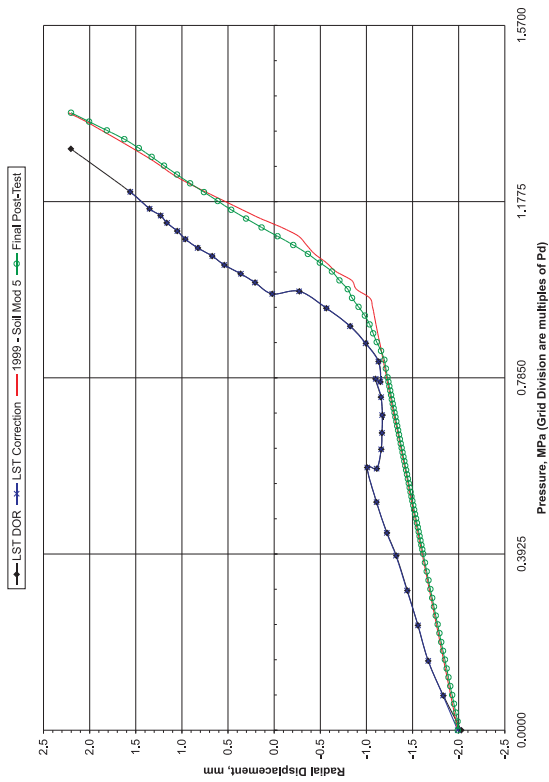
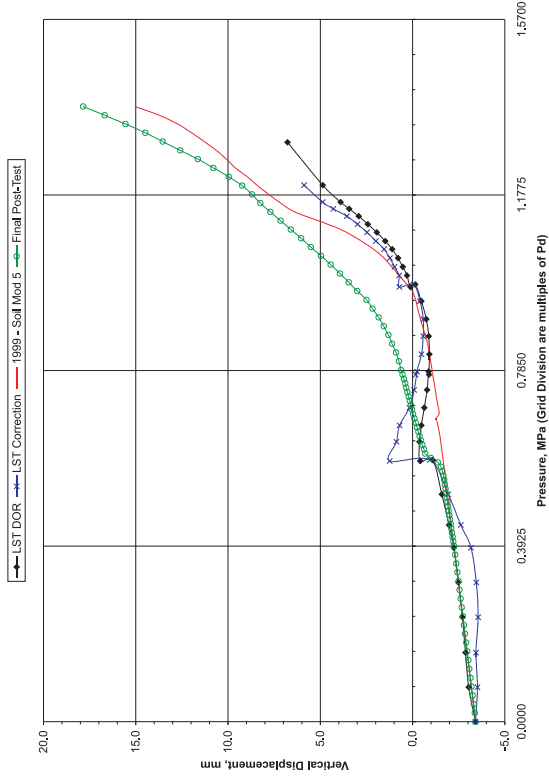


Figure 5-14. Comparisons at Standard Output Location 5, 6, 7, and 8

Standard Output Location #9. Azimuth: 135 Degrees, Elevation: 14.55 Meters, Dome 45 deg



Standard Output Location #10. Azimuth: 135 Degrees, Elevation: 14.55 Meters, Dome 45 deg



Standard Output Location #11. Azimuth: 135 Degrees, Elevation: 16.13 Meters, Dome Apex

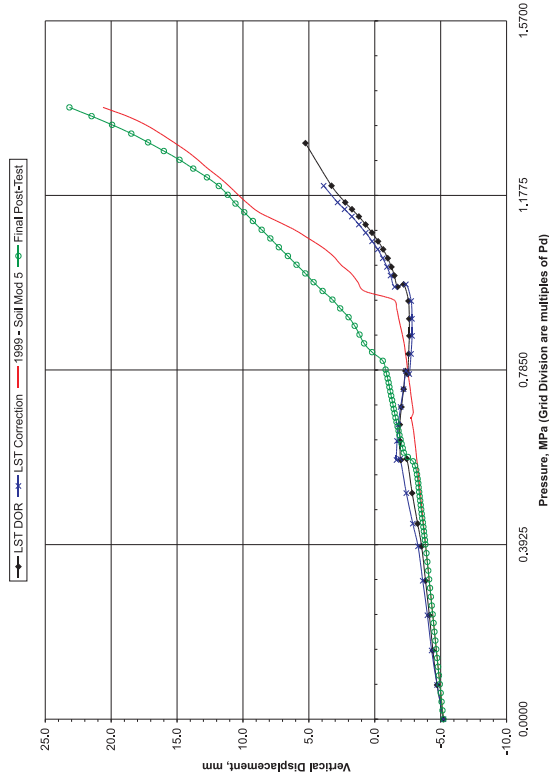
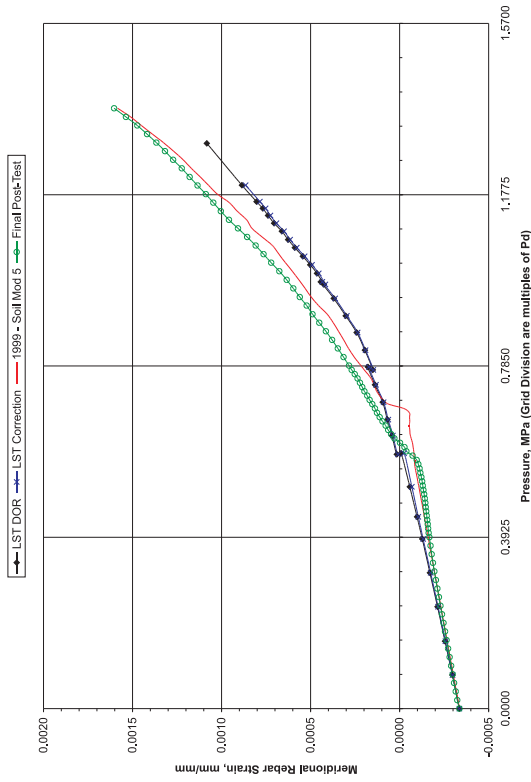
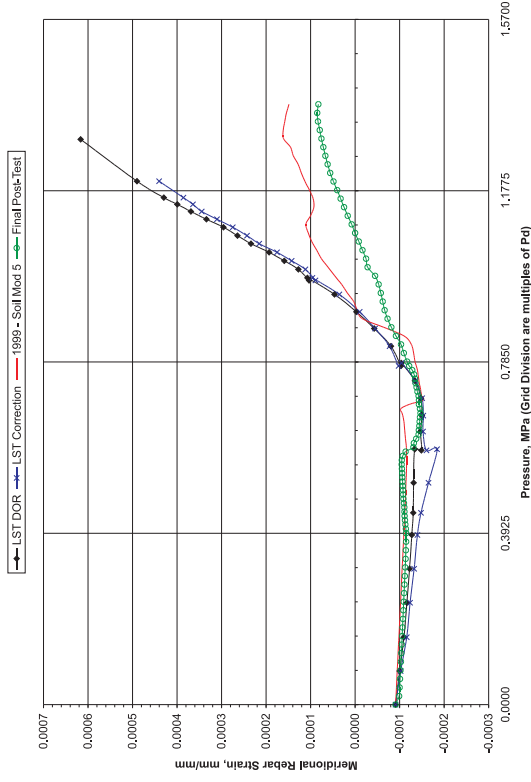


Figure 5-15. Comparisons at Standard Output Location 9, 10, and 11

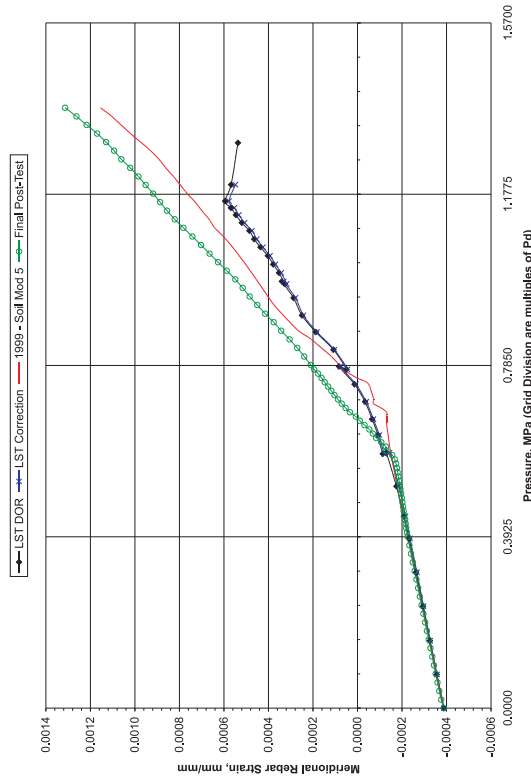
Standard Output Location #16. Azimuth: 135 Degrees, Elevation: 0.05 Meters, Inner Rebar Layer, Base of Cylinder



Standard Output Location #17. Azimuth: 135 Degrees, Elevation: 0.05 Meters, Outer Rebar Layer, Base of Cylinder



Standard Output Location #18. Azimuth: 135 Degrees, Elevation: 0.25 Meters, Inner Rebar Layer, Base of Cylinder



Standard Output Location #19. Azimuth: 135 Degrees, Elevation: 0.25 Meters, Outer Rebar Layer, Base of Cylinder

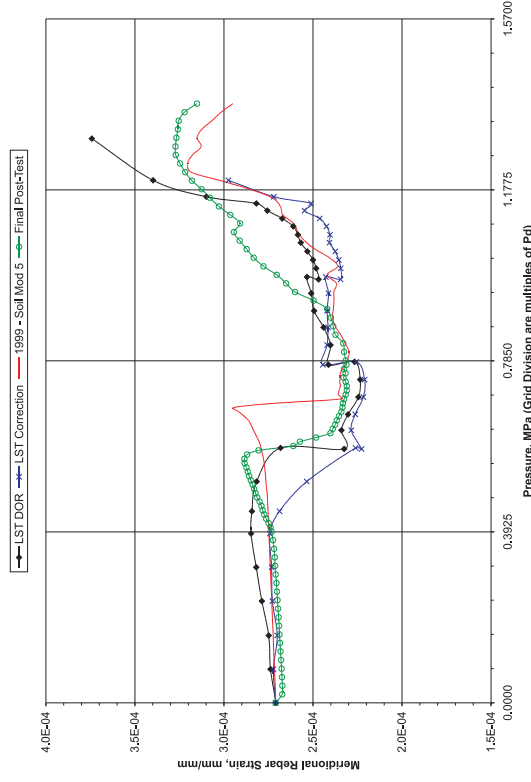
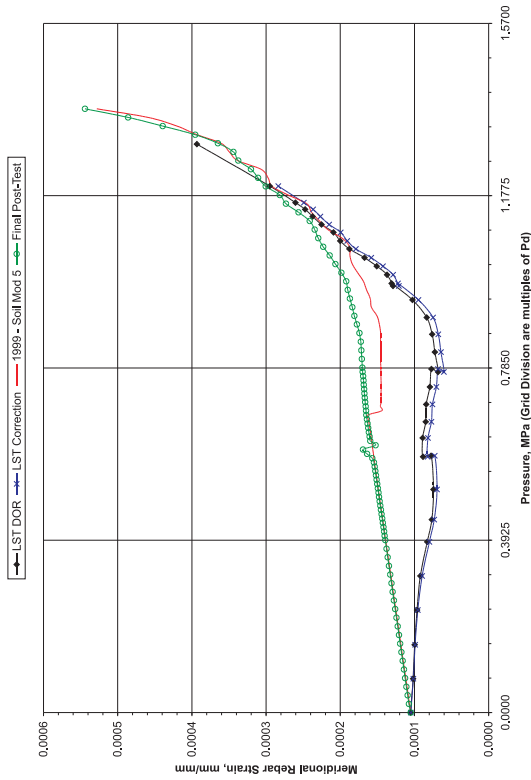
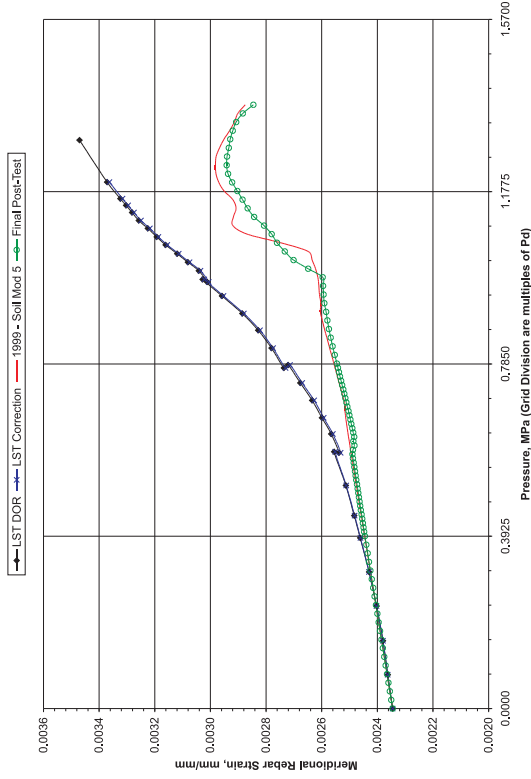


Figure 5-16. Comparisons at Standard Output Location 16, 17, 18, and 19

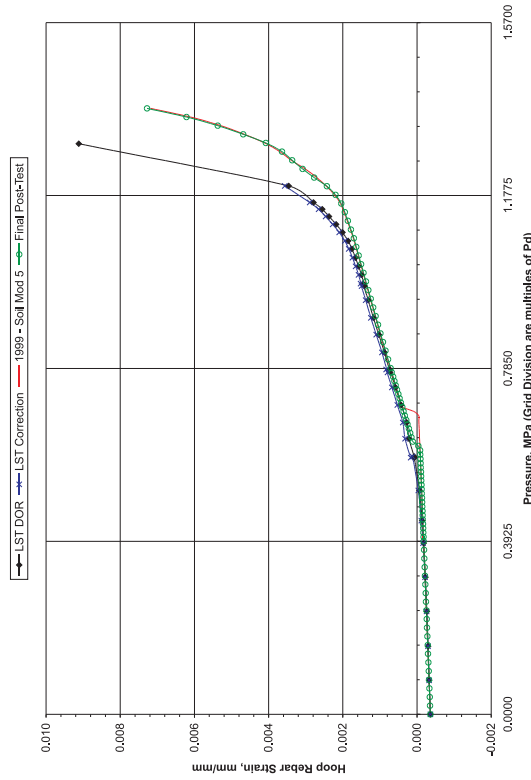
Standard Output Location #20. Azimuth: 135 Degrees, Elevation: 1.43 Meters, Inner Rebar Layer, Base of Cylinder



Standard Output Location #21. Azimuth: 135 Degrees, Elevation: 1.43 Meters, Outer Rebar Layer, Base of Cylinder



Standard Output Location #22. Azimuth: 135 Degrees, Elevation: 6.20 Meters, Outer Rebar Layer, Midheight



Standard Output Location #23. Azimuth: 135 Degrees, Elevation: 6.20 Meters, Outer Rebar Layer, Midheight

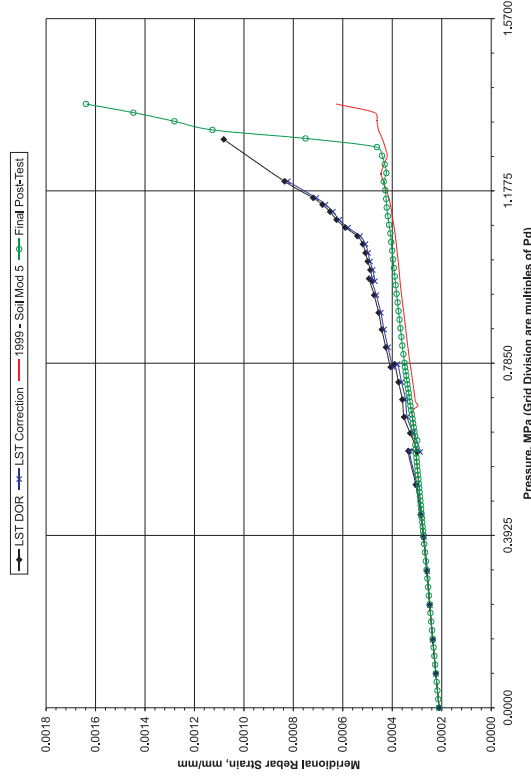
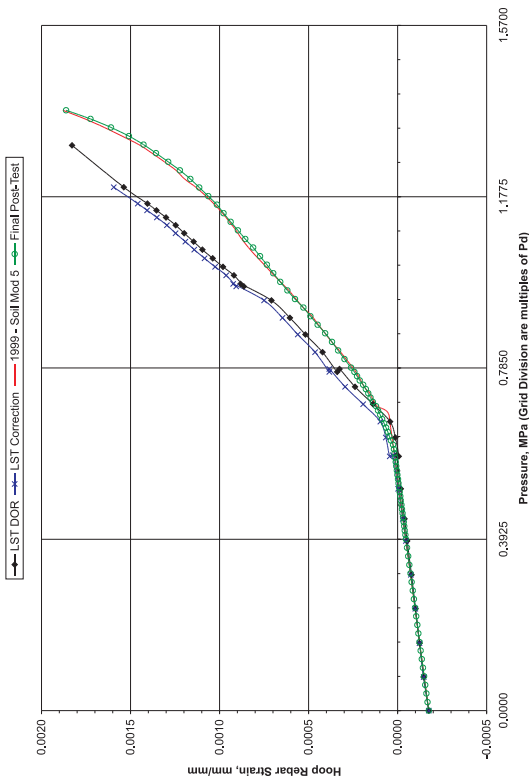
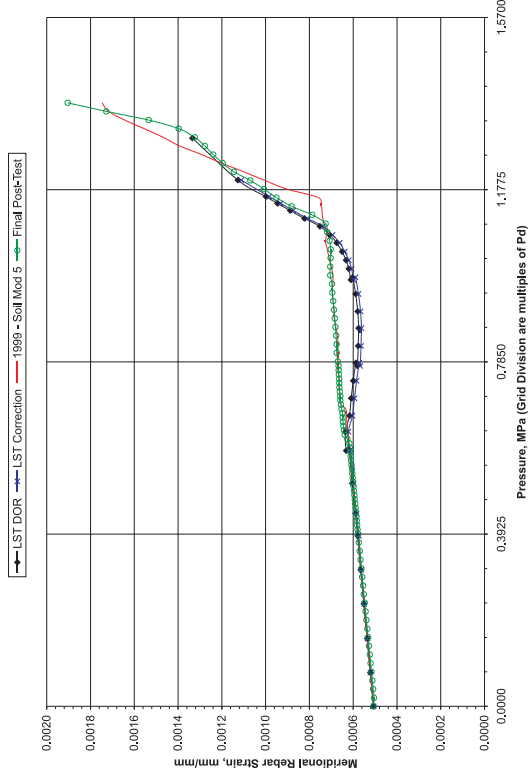


Figure 5-17. Comparisons at Standard Output Location 20, 21, 22, and 23

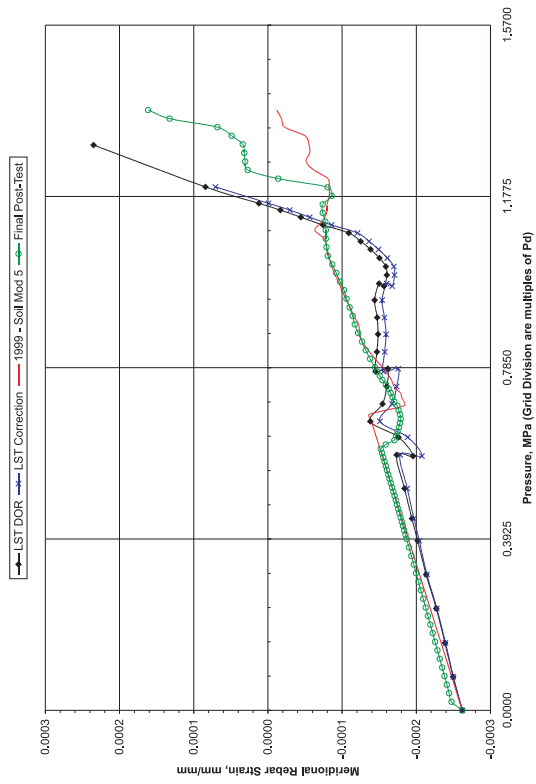
Standard Output Location #24. Azimuth: 135 Degrees, Elevation: 10.75 Meters, Outer Rebar Layer, Springline



Standard Output Location #25. Azimuth: 135 Degrees, Elevation: 10.75 Meters, Inner Rebar Layer, Springline



Standard Output Location #26. Azimuth: 135 Degrees, Elevation: 10.75 Meters, Outer Rebar Layer, Springline



Standard Output Location #27. Azimuth: 135 Degrees, Elevation: 14.55 Meters, Outer Rebar Layer, Dome 45 deg

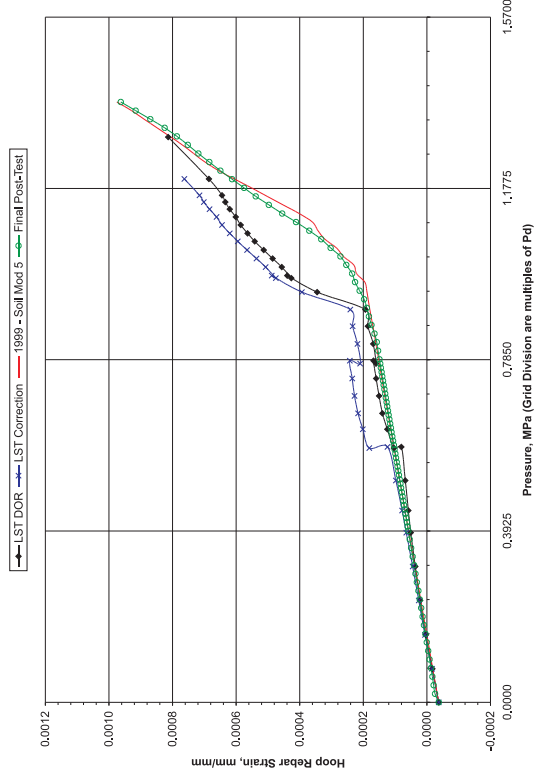
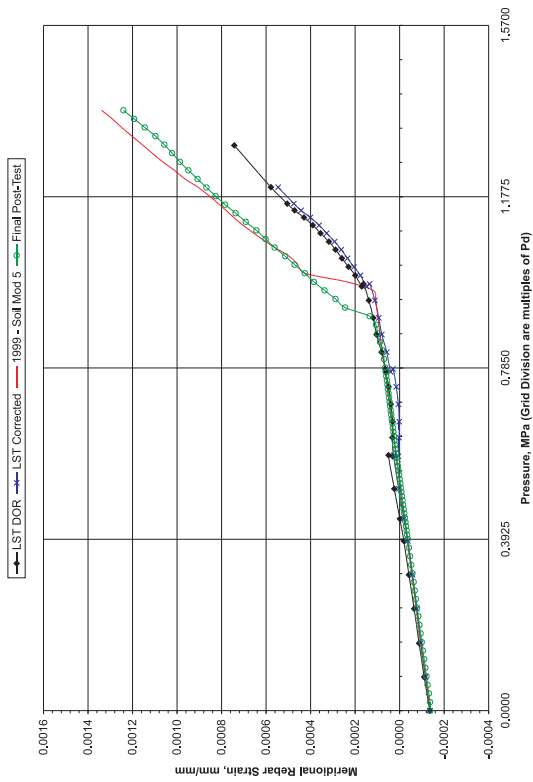


Figure 5-18. Comparisons at Standard Output Location 24, 25, 26, and 27

Standard Output Location #28. Azimuth: 135 Degrees, Elevation: 14.55 Meters.
Inner Rebar Layer, Dome 45 deg



Standard Output Location #29. Azimuth: 135 Degrees, Elevation: 14.55 Meters.
Outer Rebar Layer, Dome 45 deg

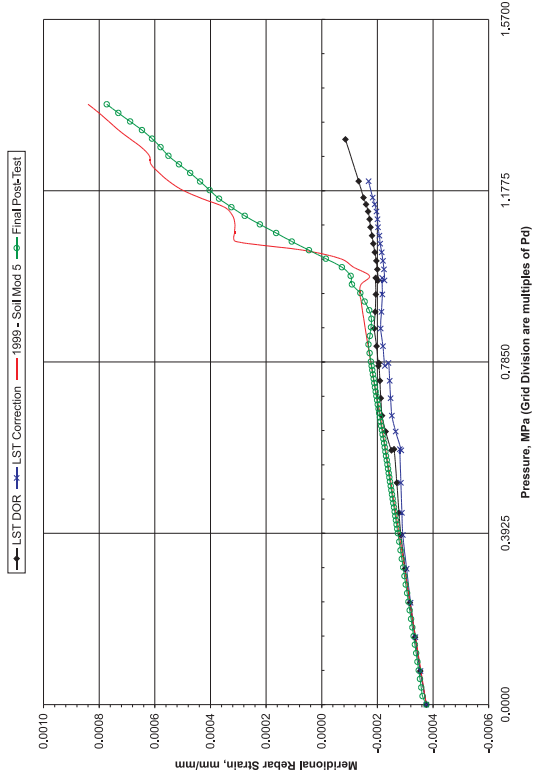
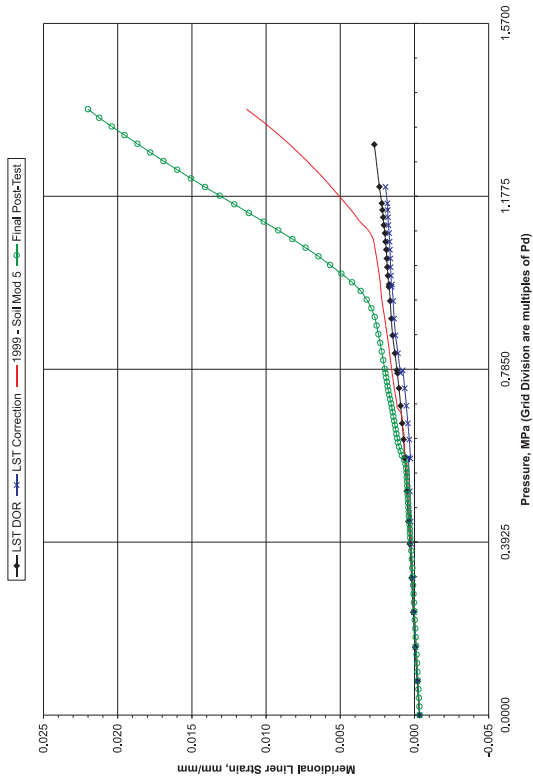
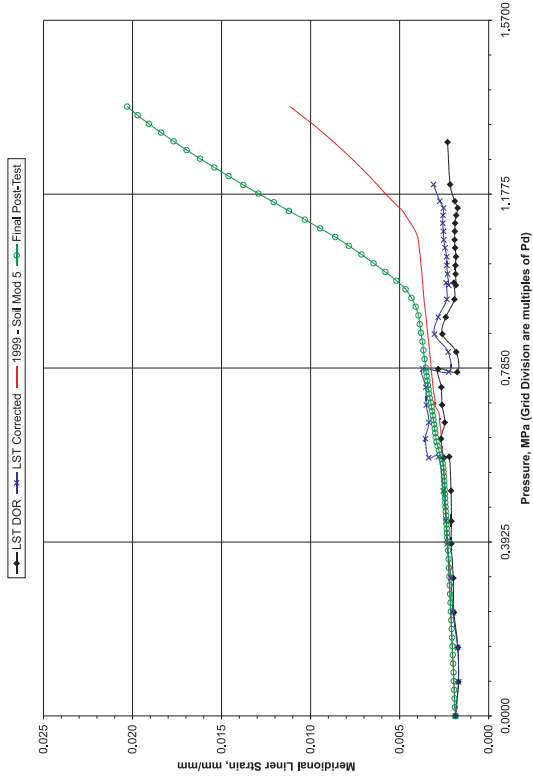


Figure 5-19. Comparisons at Standard Output Location 28 and 29

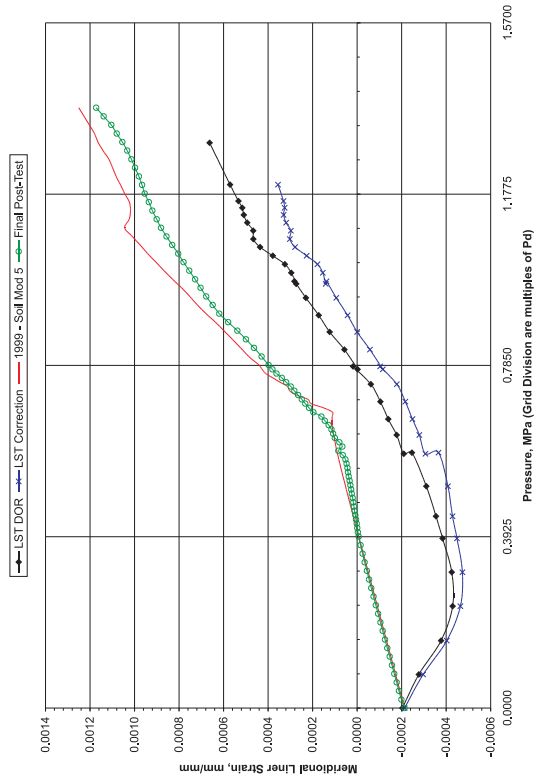
Standard Output Location #34. Azimuth: 0 Degrees, Elevation: 0.01 Meters, Inside Liner Surface, Base of Cylinder



Standard Output Location #35. Azimuth: 0 Degrees, Elevation: 0.01 Meters, Outside Liner Surface, Base of Cylinder



Standard Output Location #36. Azimuth: 135 Degrees, Elevation: 0.25 Meters, Inside Liner Surface, Base of Cylinder



Standard Output Location #37. Azimuth: 135 Degrees, Elevation: 0.25 Meters, Inside Liner Surface, Base of Cylinder

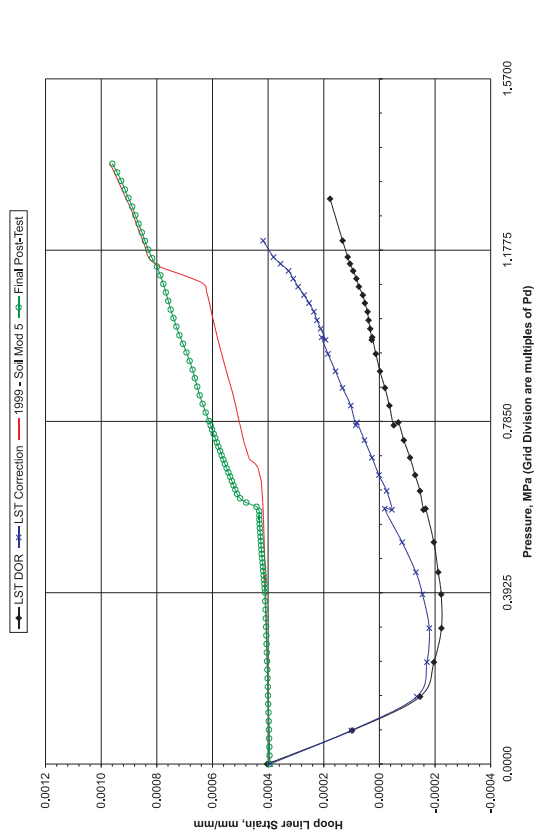
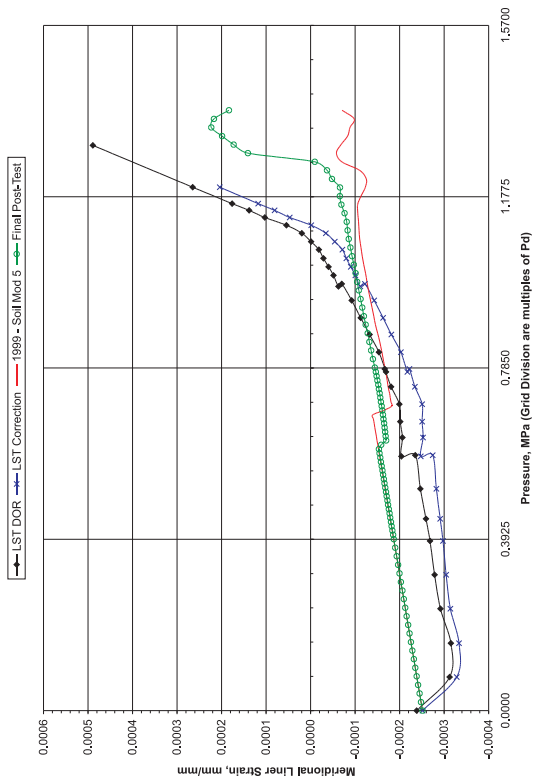
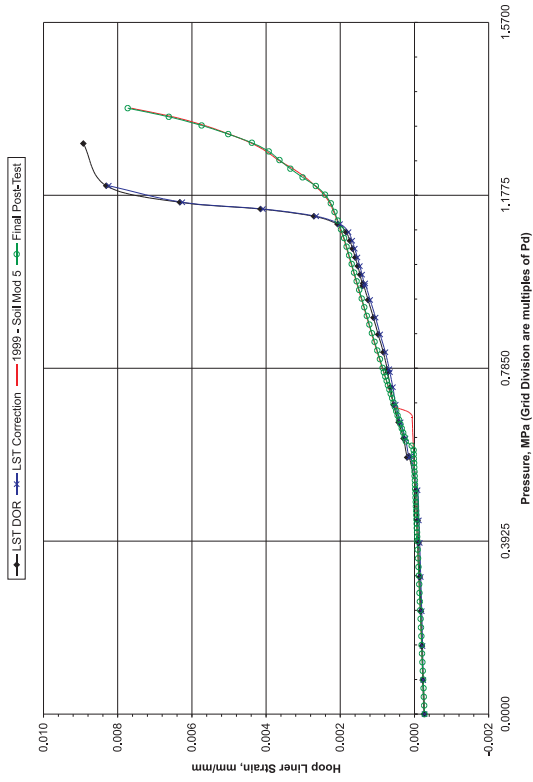


Figure 5-20. Comparisons at Standard Output Location 34, 35, 36, and 37

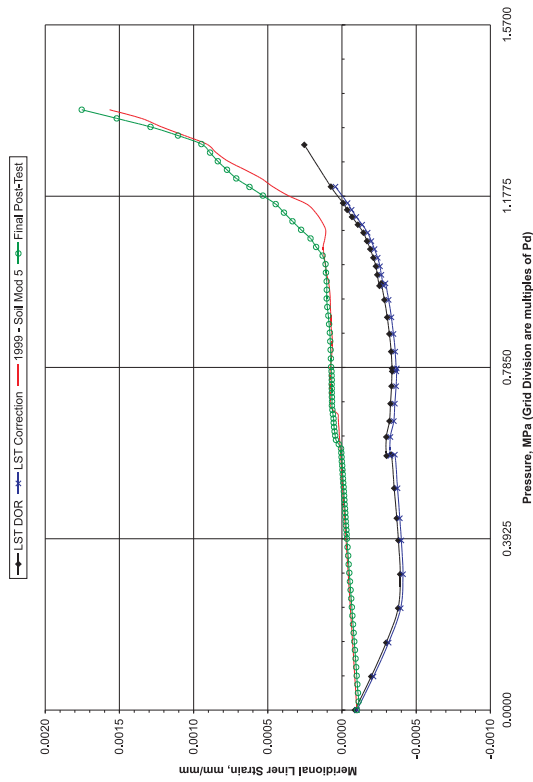
Standard Output Location #38. Azimuth: 135 Degrees, Elevation: 6.20 Meters, Inside Liner Surface, Midheight



Standard Output Location #39. Azimuth: 135 Degrees, Elevation: 6.20 Meters, Inside Liner Surface, Midheight



Standard Output Location #40. Azimuth: 135 Degrees, Elevation: 10.75 Meters, Inside Liner Surface, Springline



Standard Output Location #41. Azimuth: 135 Degrees, Elevation: 10.75 Meters, Inside Liner Surface, Springline

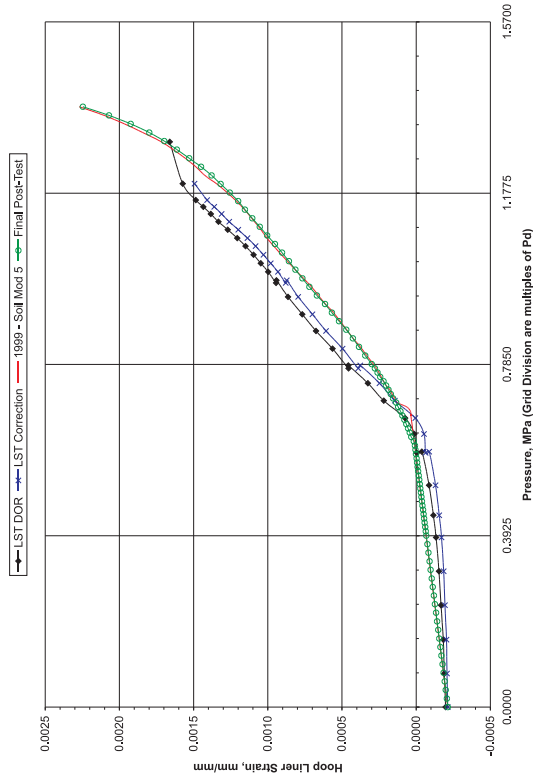


Figure 5-21. Comparisons at Standard Output Location 38, 39, 40, and 41

Standard Output Location #42. Azimuth: 135 Degrees, Elevation: 16.13 Meters,
Inside Liner Surface, Dome Apex

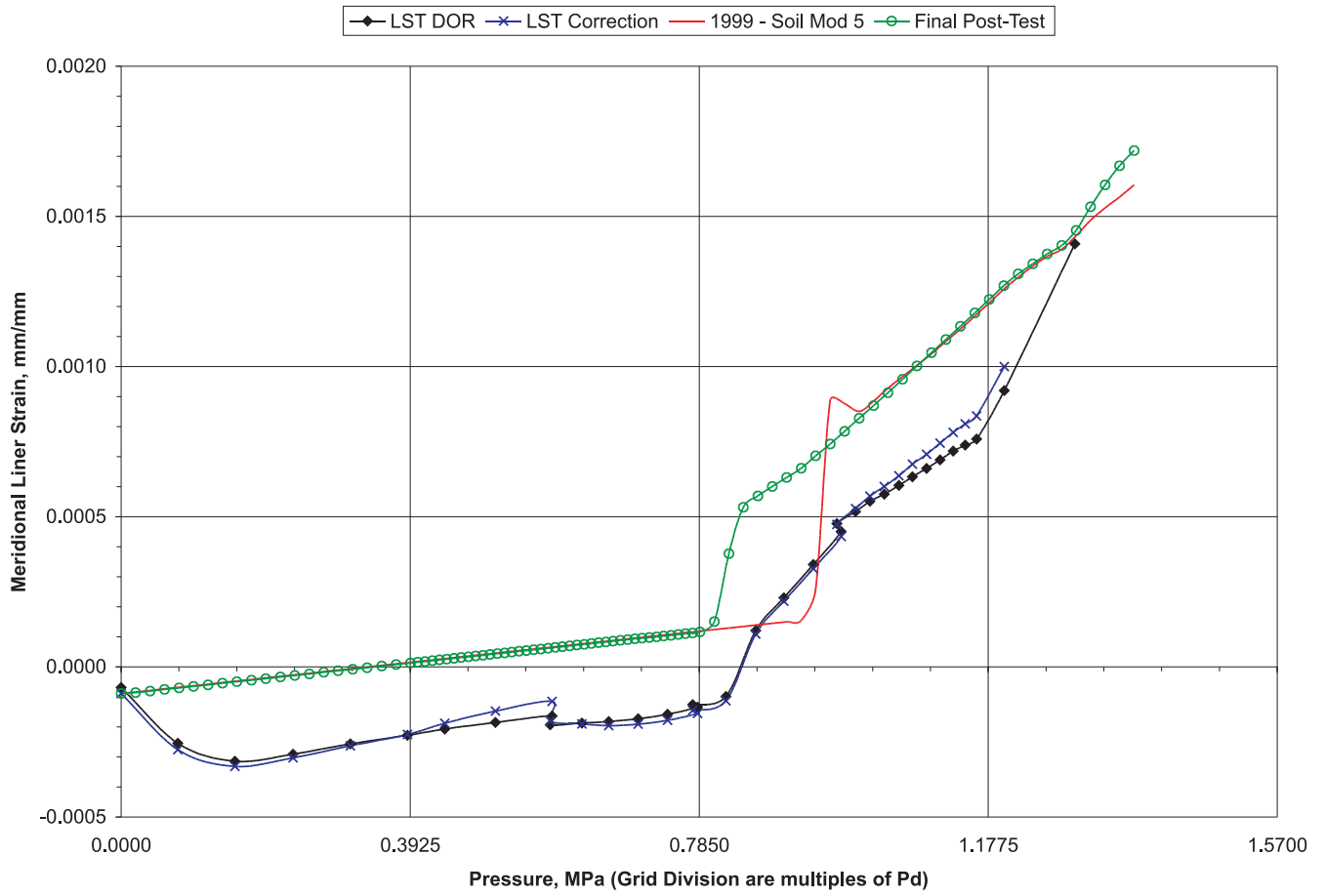


Figure 5-22. Comparisons at Standard Output Location 42

Standard Output Location #49. Azimuth: 135 Degrees, Elevation: 10.75 Meters,
Tendon - V46, Tendon Springline

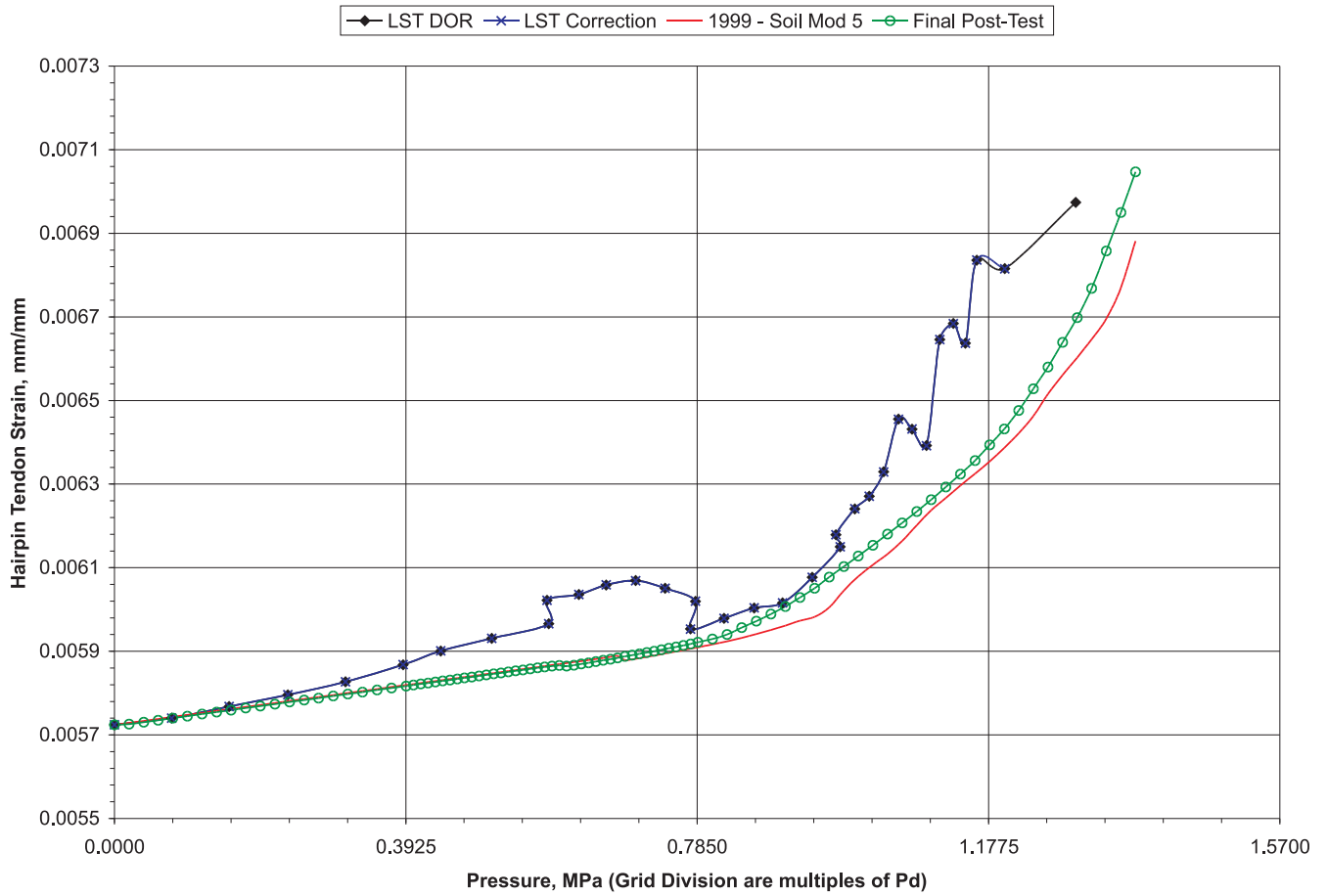


Figure 5-23. Comparisons at Standard Output Location 49

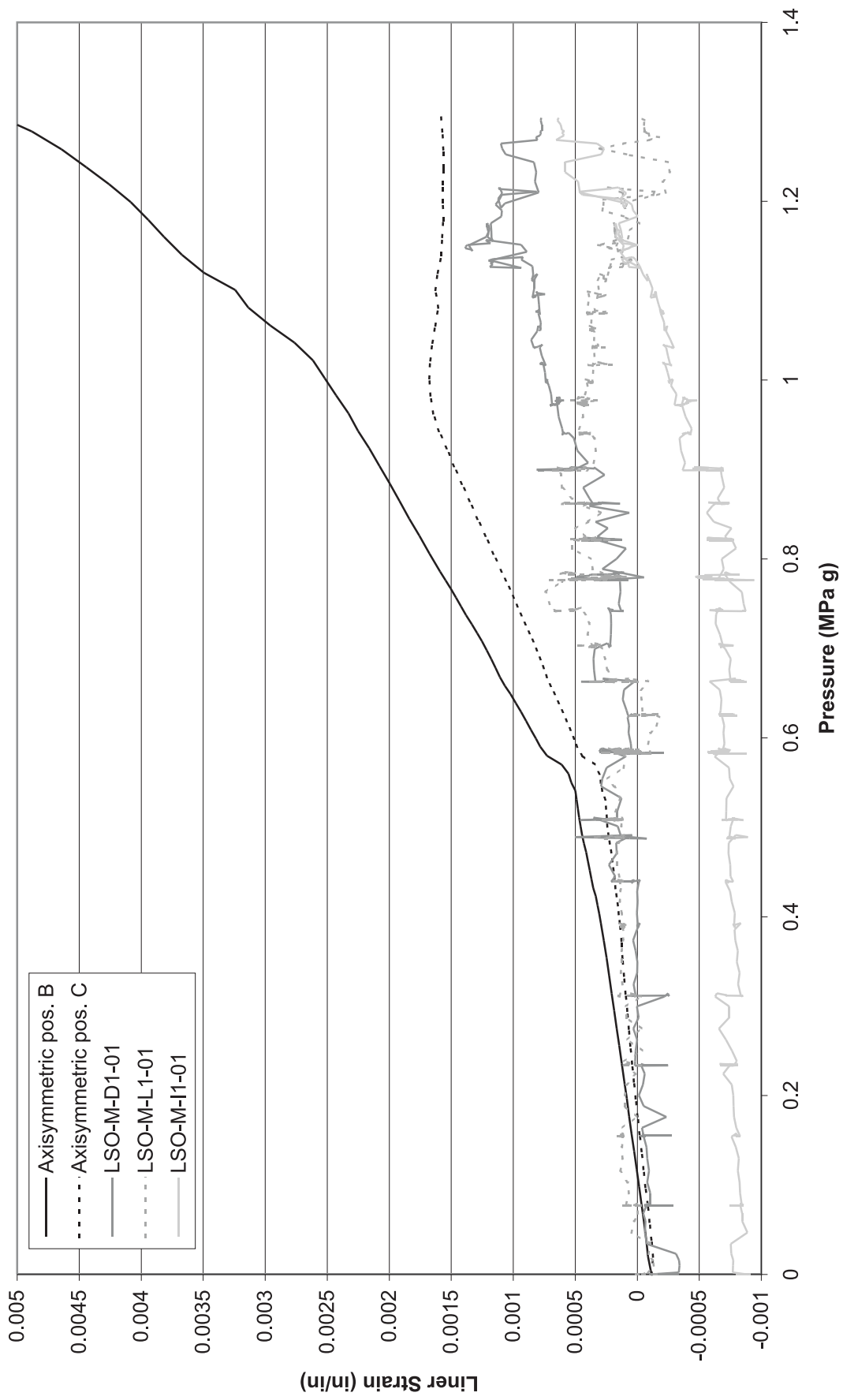


Figure 5-24. Final Posttest Analysis Vs. LST at Wall Base Liner Position B-C

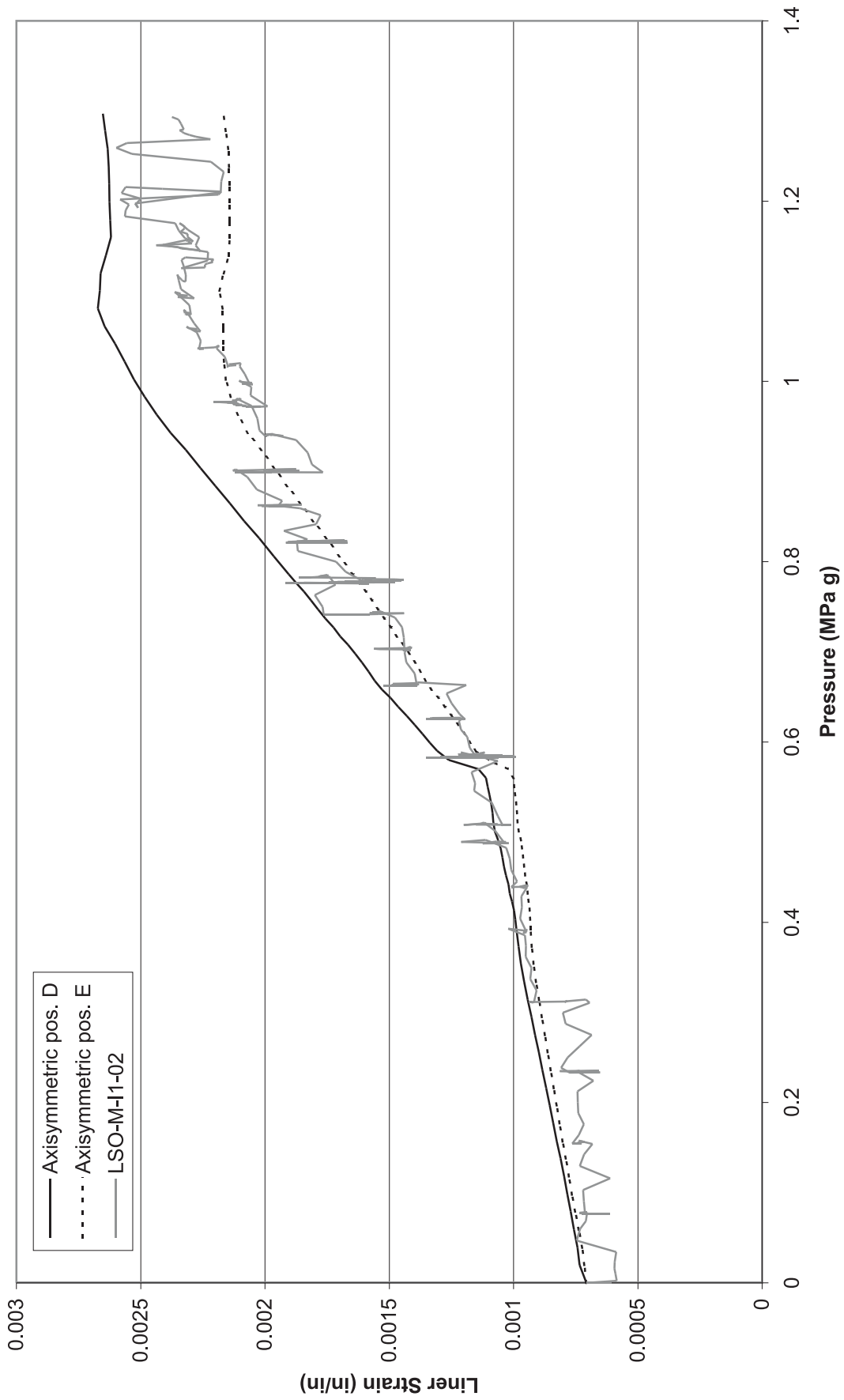


Figure 5-25. Final Posttest Analysis Vs. LST at Wall Base Liner Position D-E

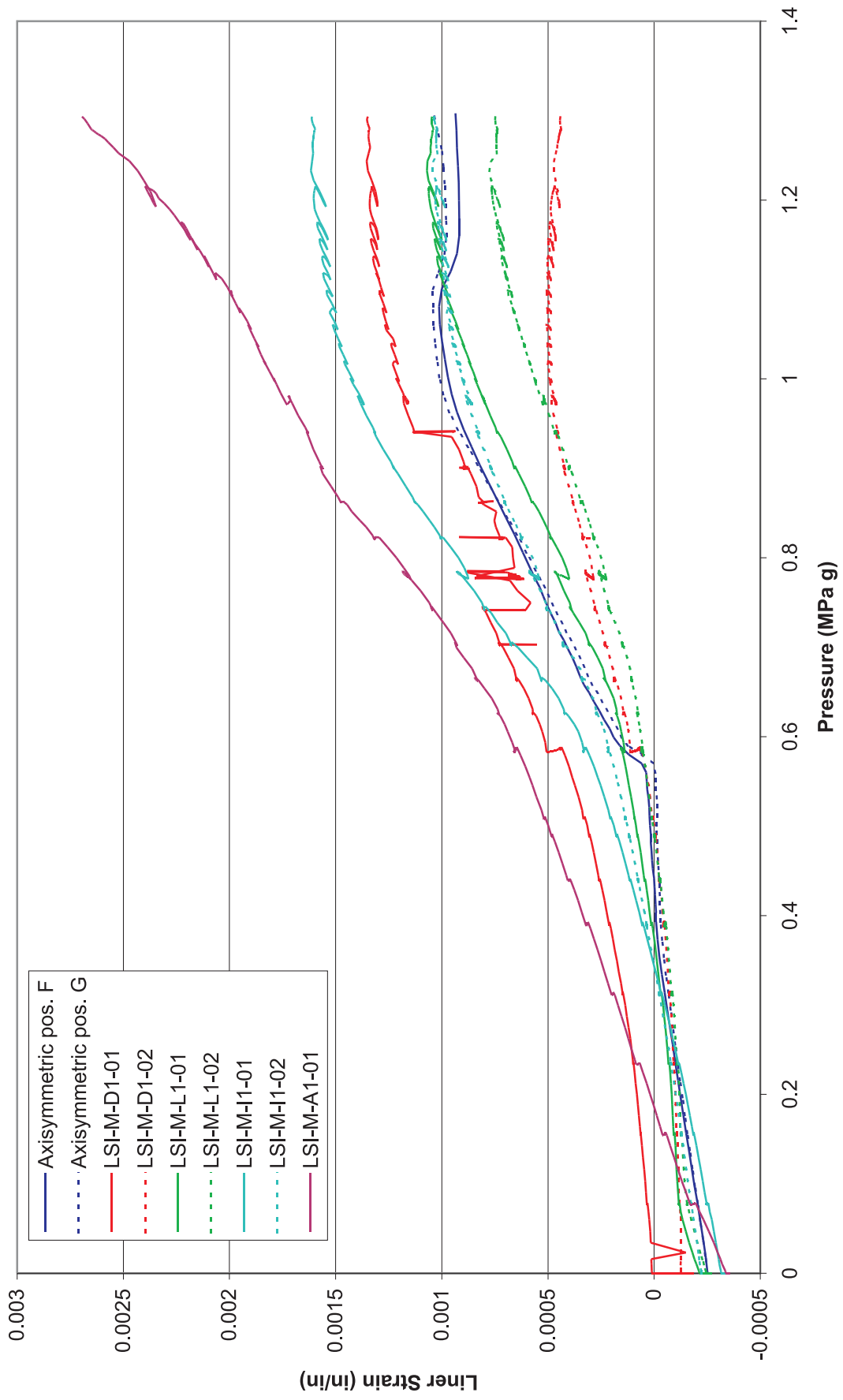


Figure 5-26. Final Posttest Analysis Vs. LST at Wall Base Liner Position F-G

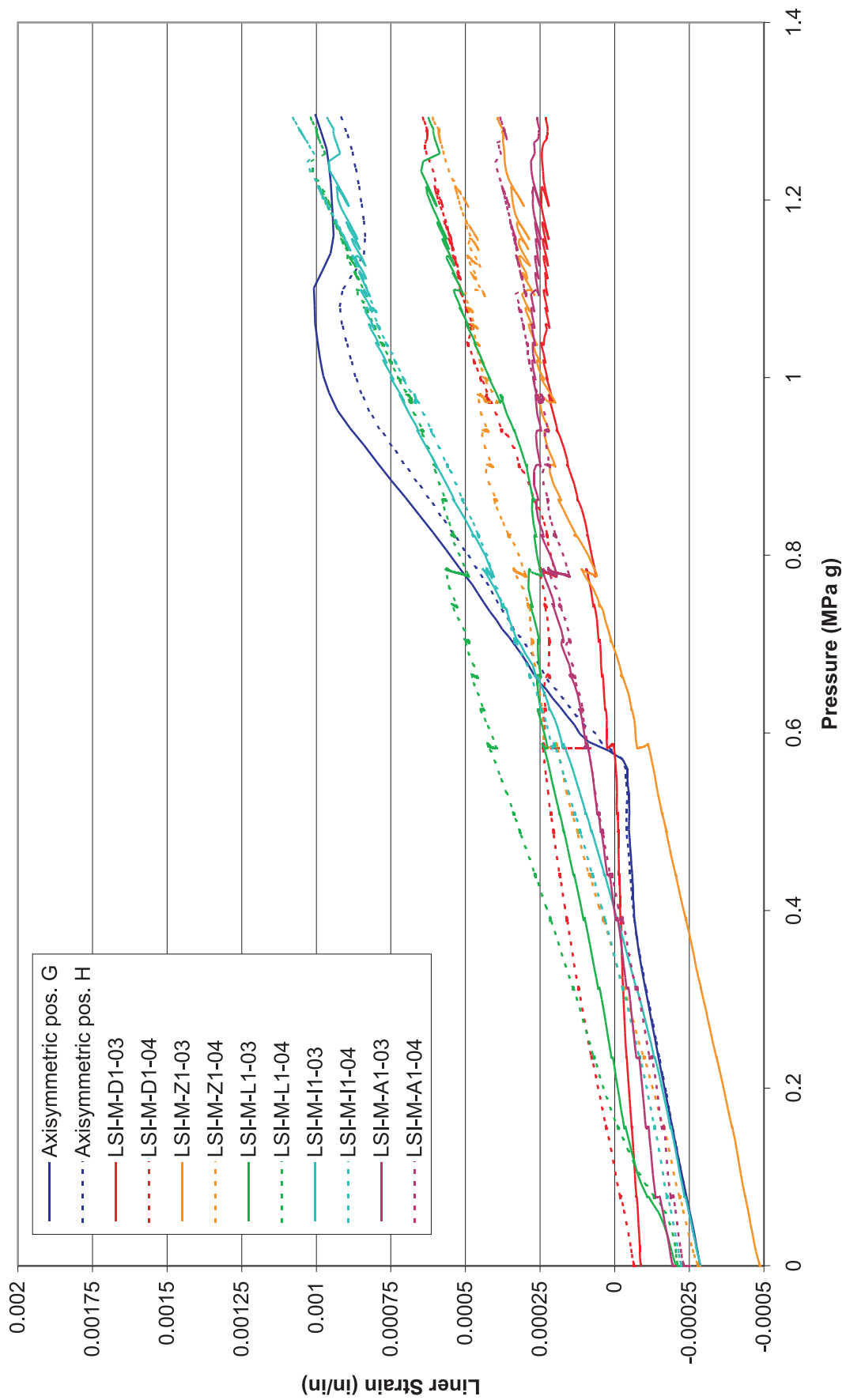


Figure 5-27. Final Posttest Analysis Vs. LST at Wall Base Liner Position G-H

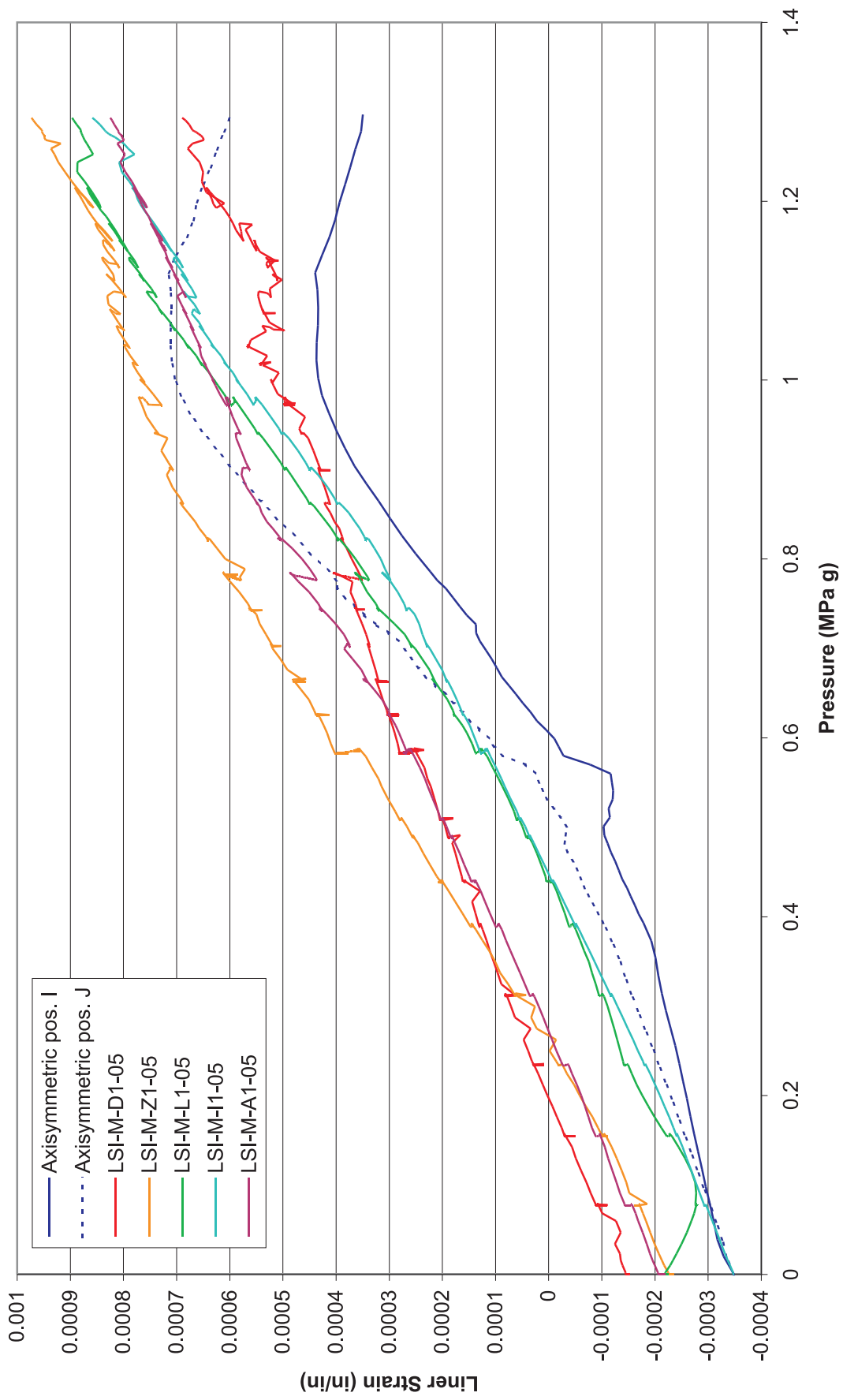


Figure 5-28. Final Posttest Analysis Vs. LST at Wall Base Liner Position I-J

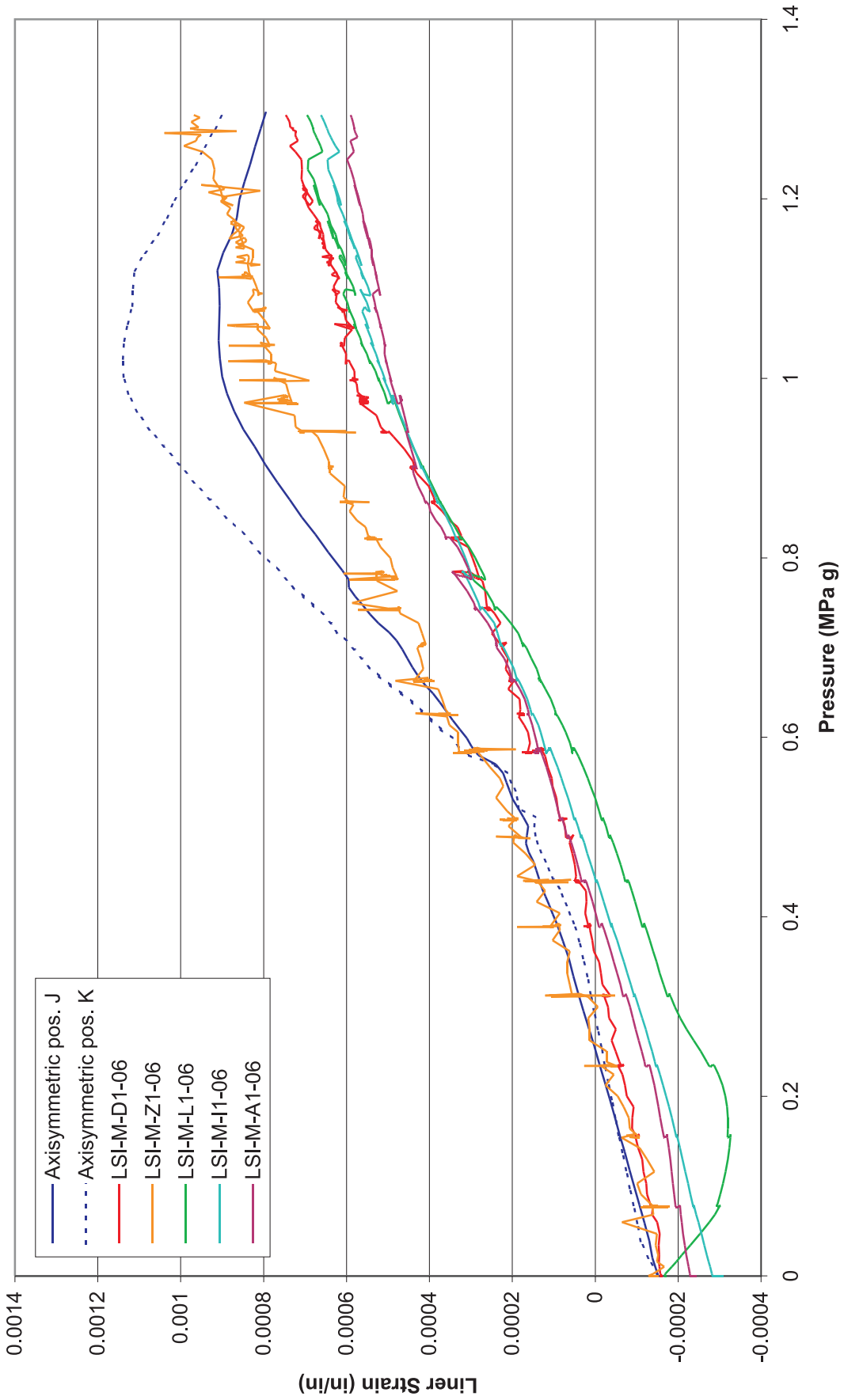


Figure 5-29. Final Posttest Analysis Vs. LST at Wall Base Liner Position J-K

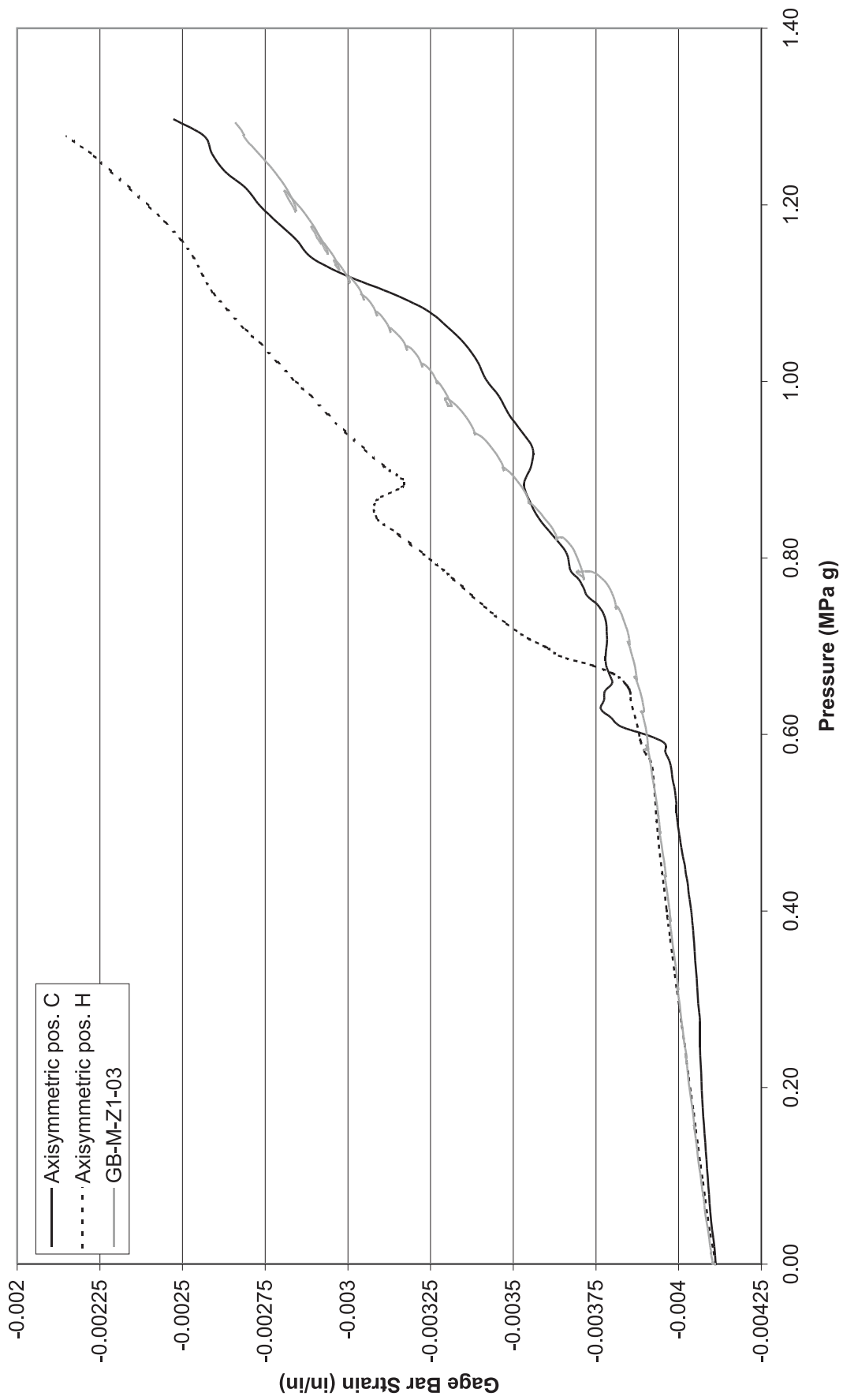


Figure 5-30. Final Posttest Analysis Vs. LST at Wall Base Gage Bar Position C-H

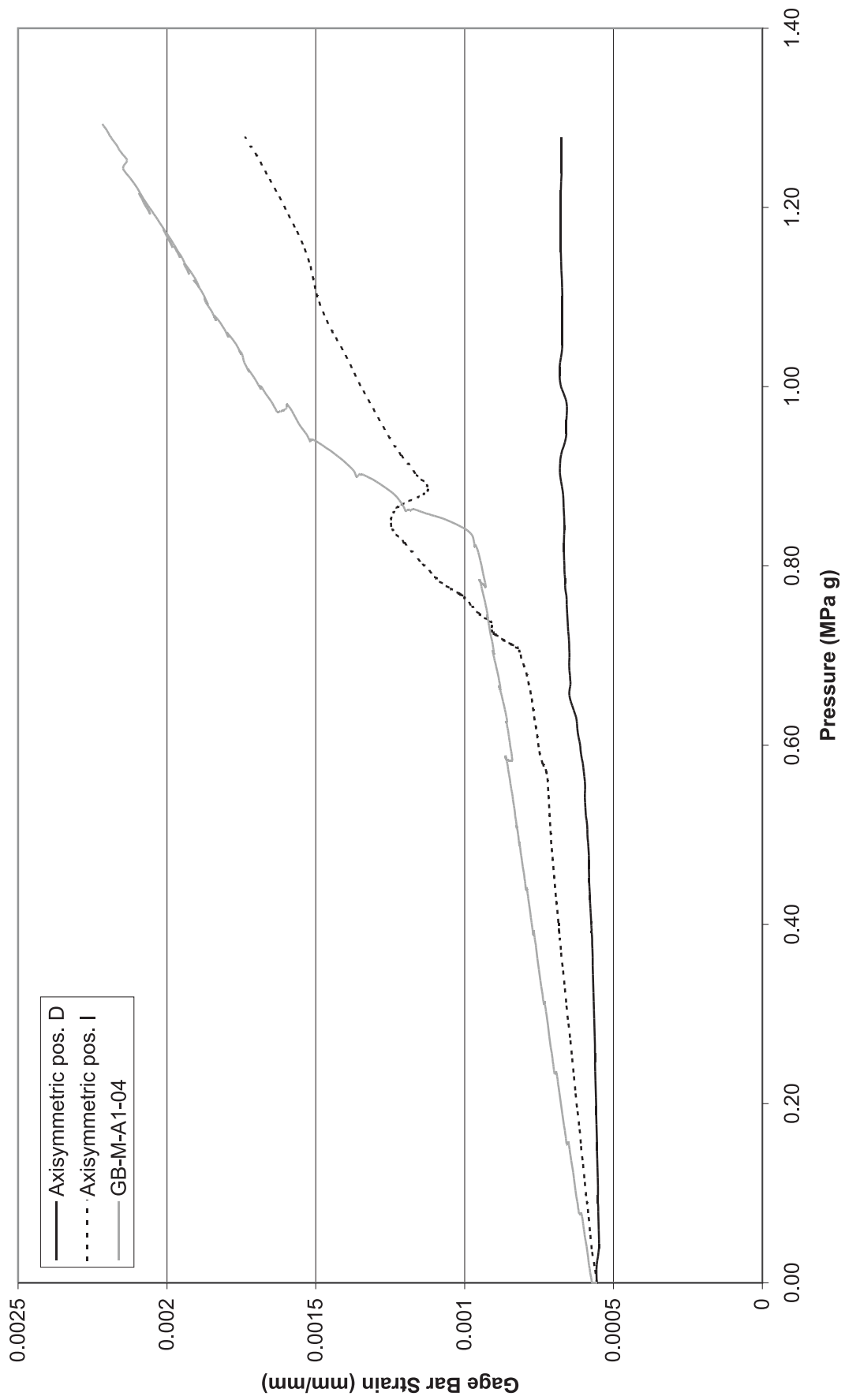


Figure 5-31. Final Posttest Analysis Vs. LST at Wall Base Gage Bar Position D-I

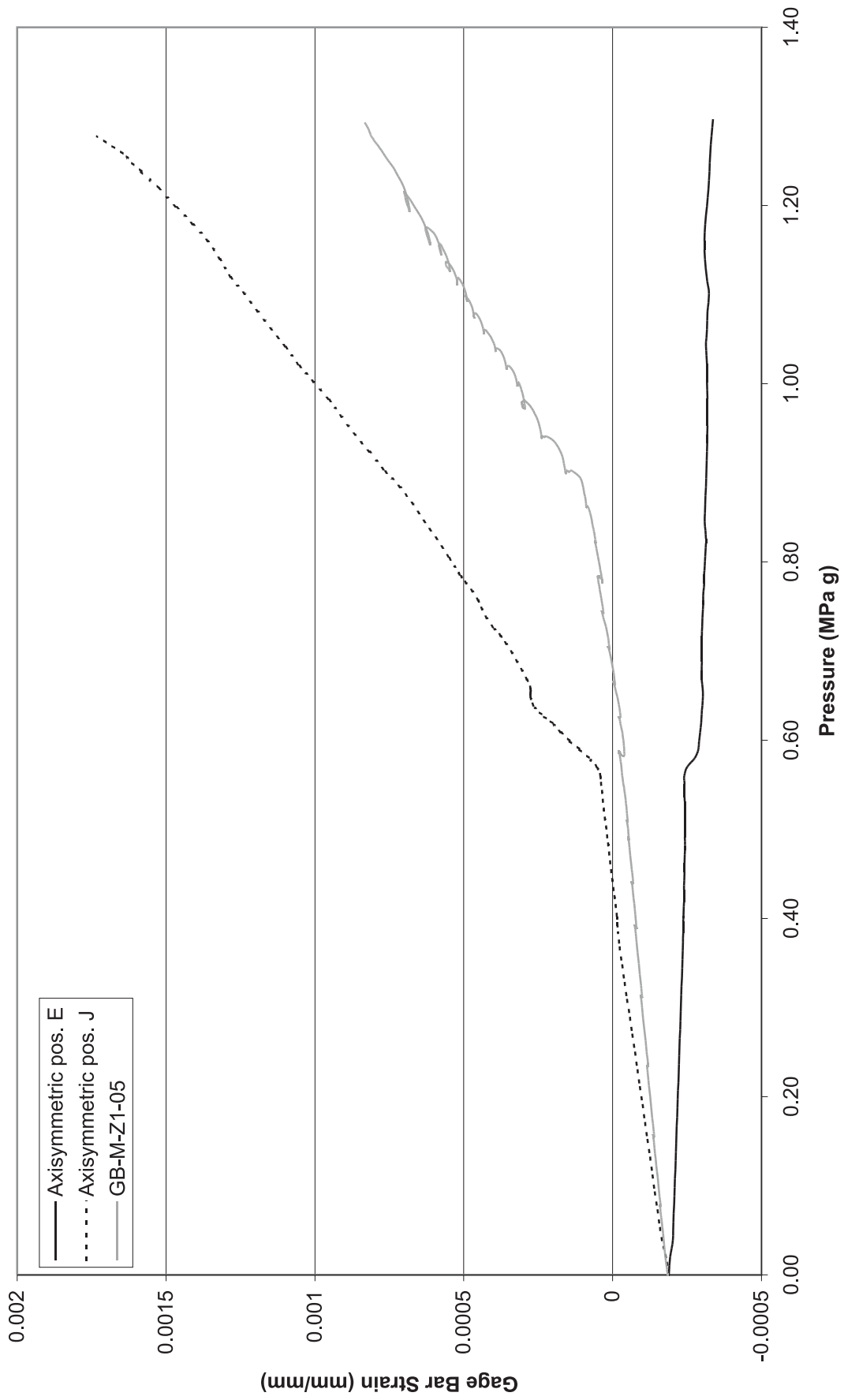


Figure 5-32. Final Posttest Analysis Vs. LST at Wall Base Gage Bar Position E-J

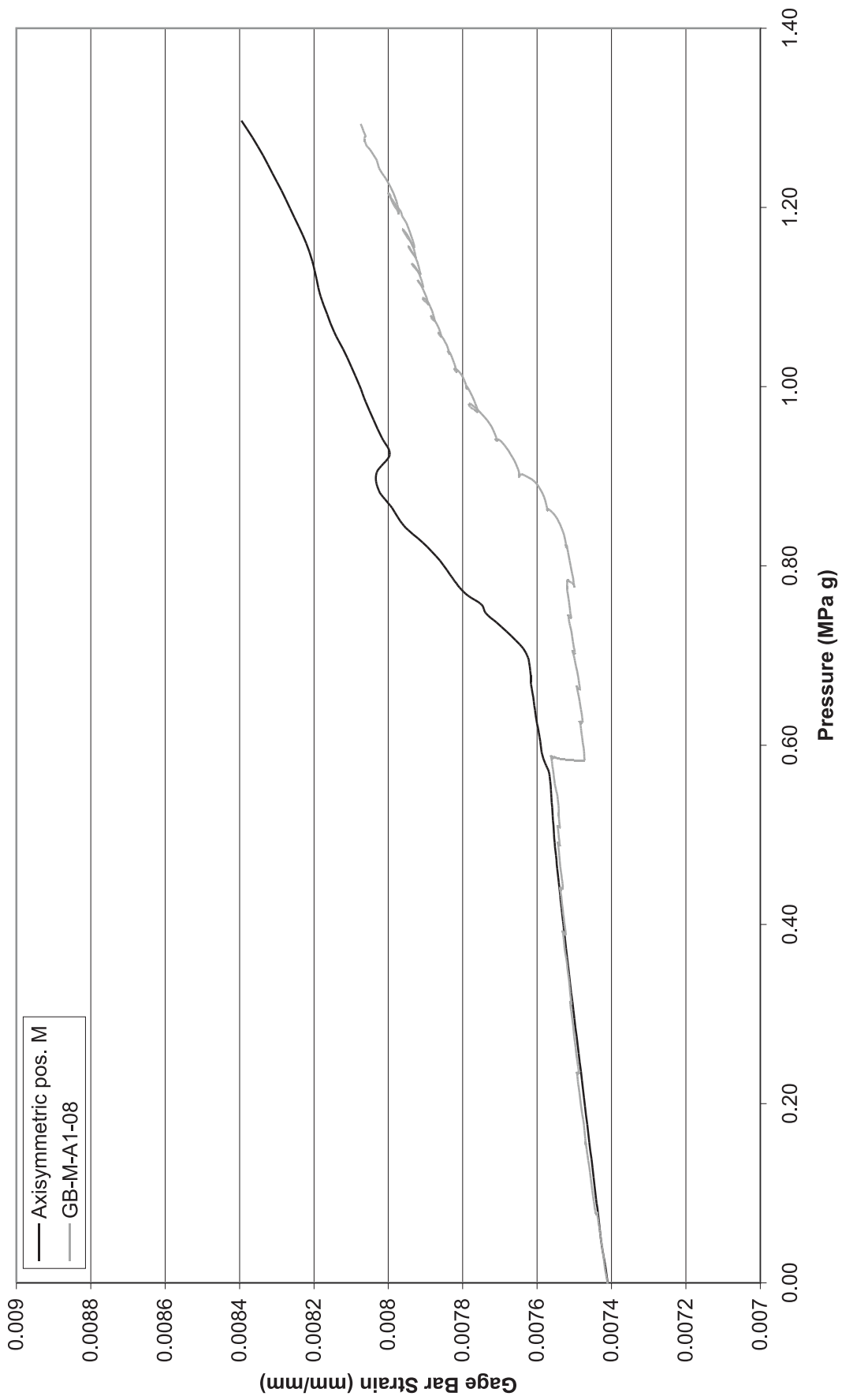


Figure 5-33. Final Pos-test Analysis Vs. LST at Wall Base Gage Bar Position M

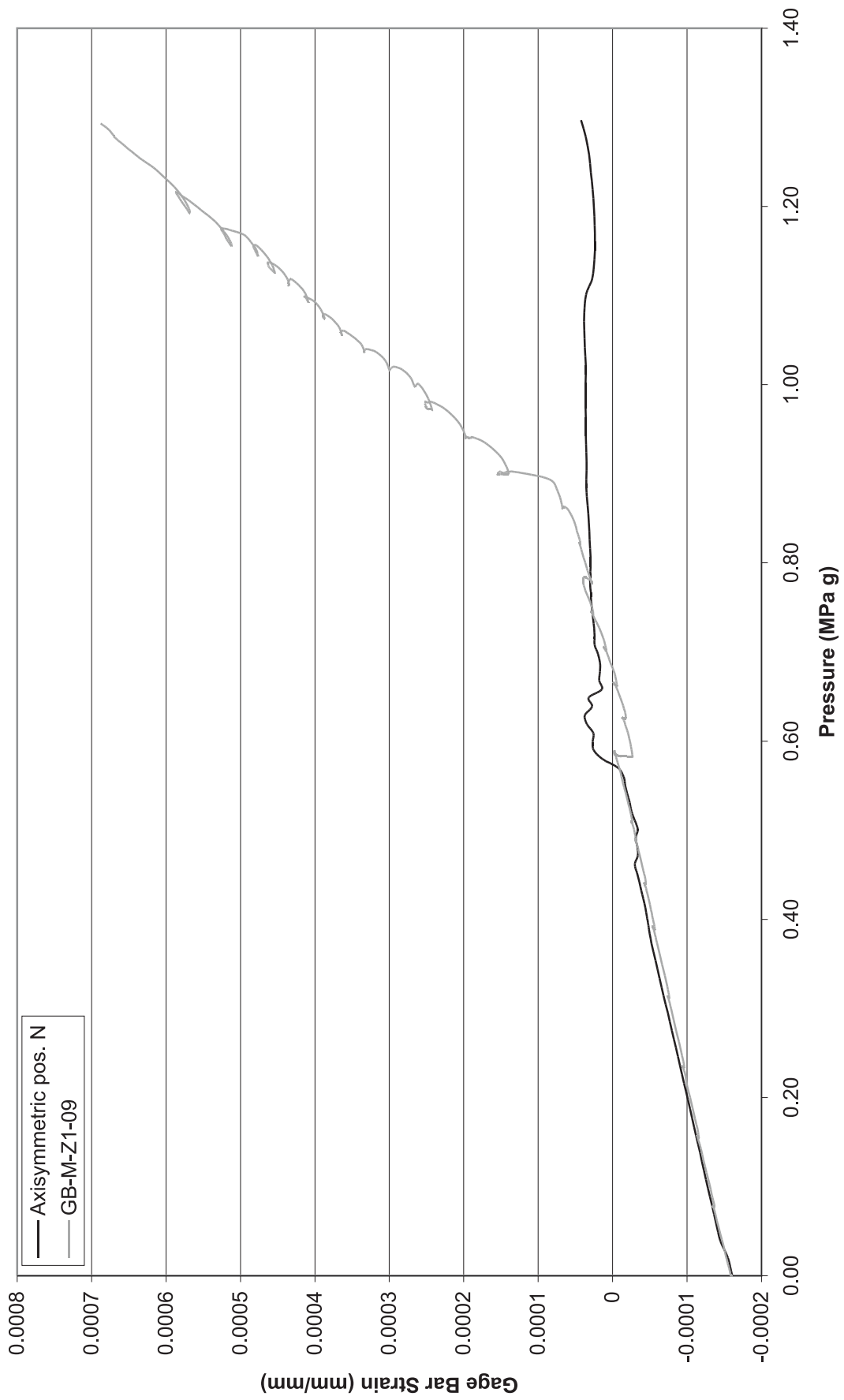


Figure 5-34. Final Posttest Analysis Vs. LST at Wall Base Gage Bar Position N

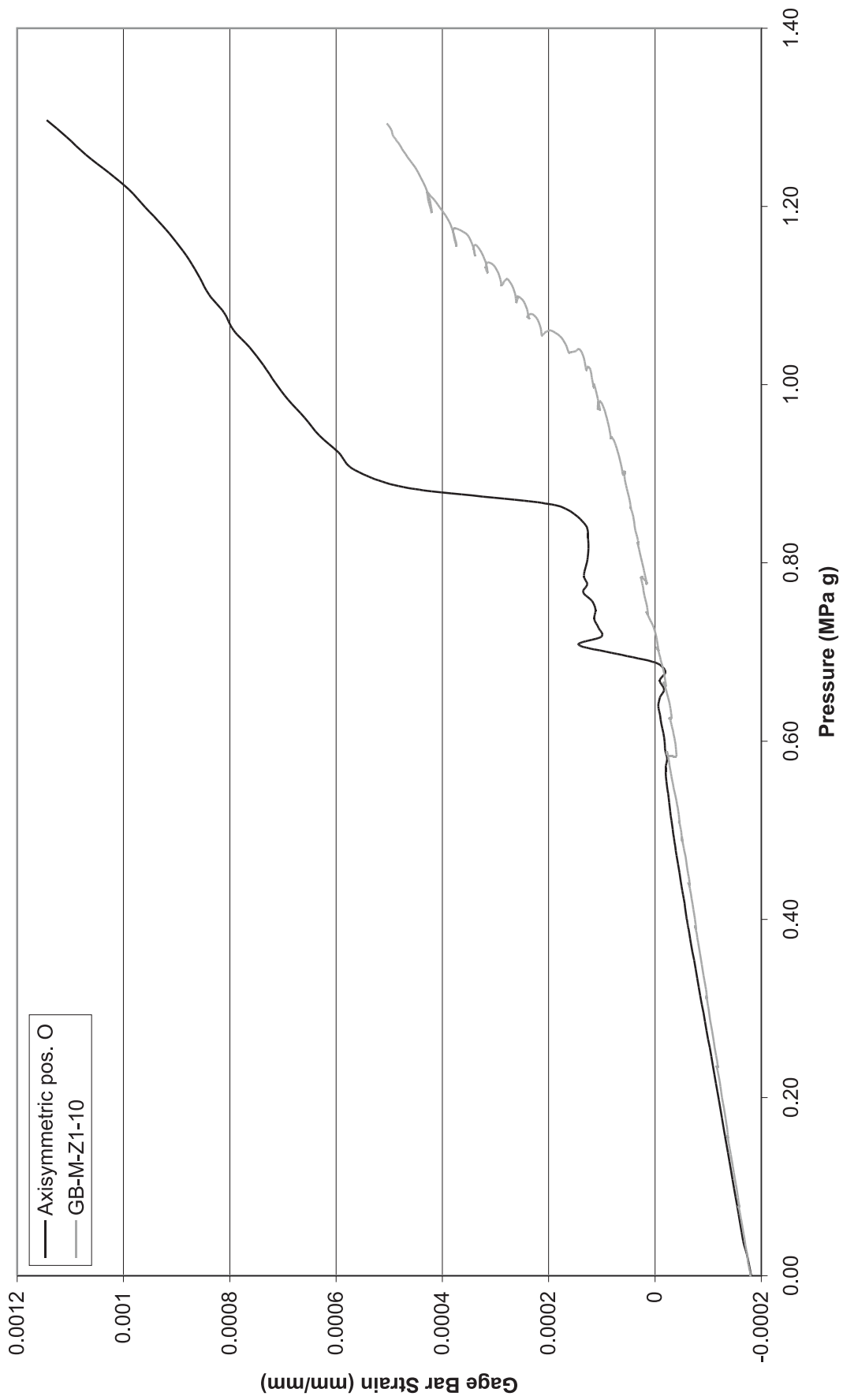


Figure 5-35. Final Posttest Analysis Vs. LST at Wall Base Gage Bar Position O

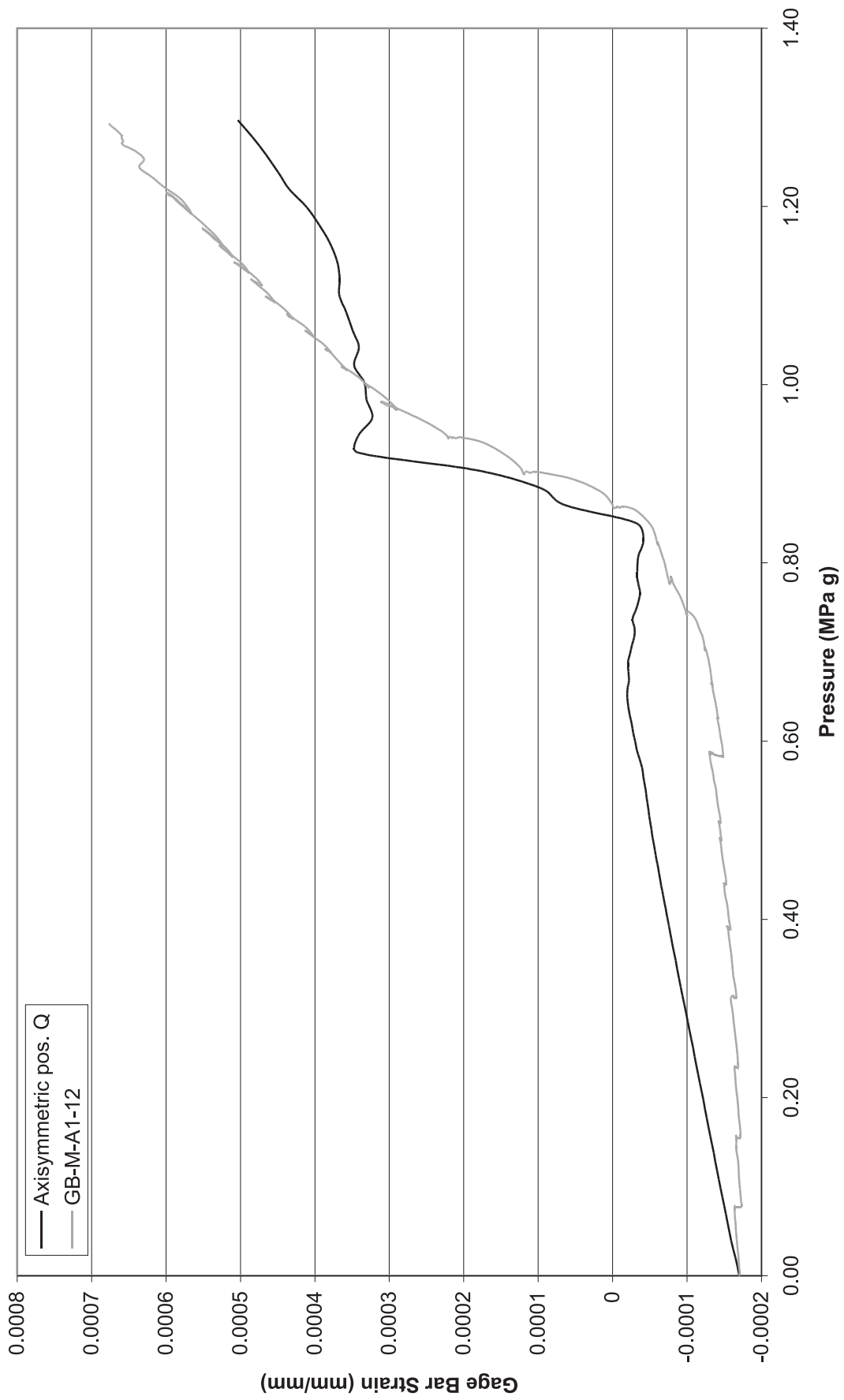


Figure 5-36. Final Posttest Analysis Vs. LST at Wall Base Gage Bar Position Q

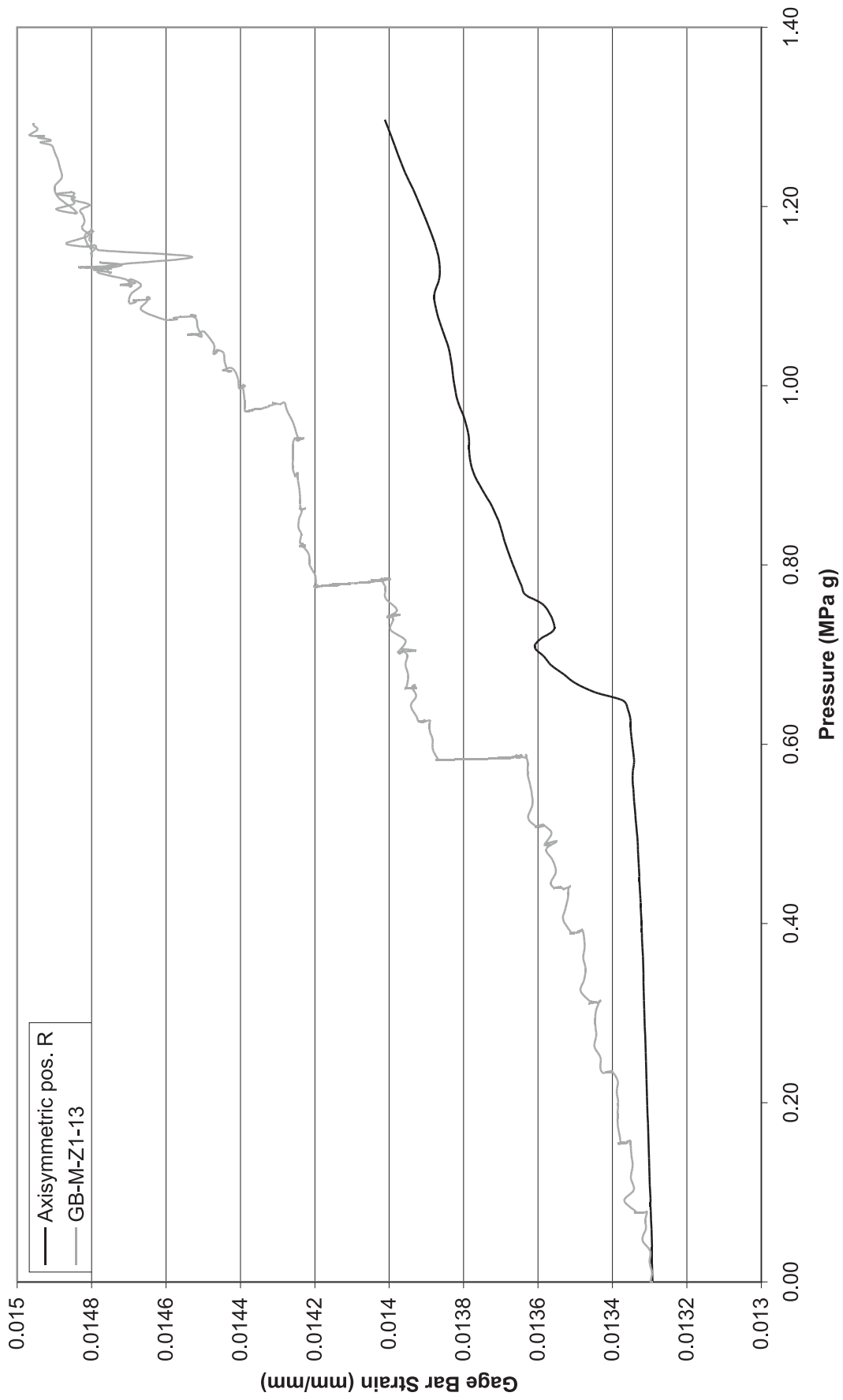


Figure 5-37. Final Posttest Analysis Vs. LST at Wall Base Gage Bar Position R

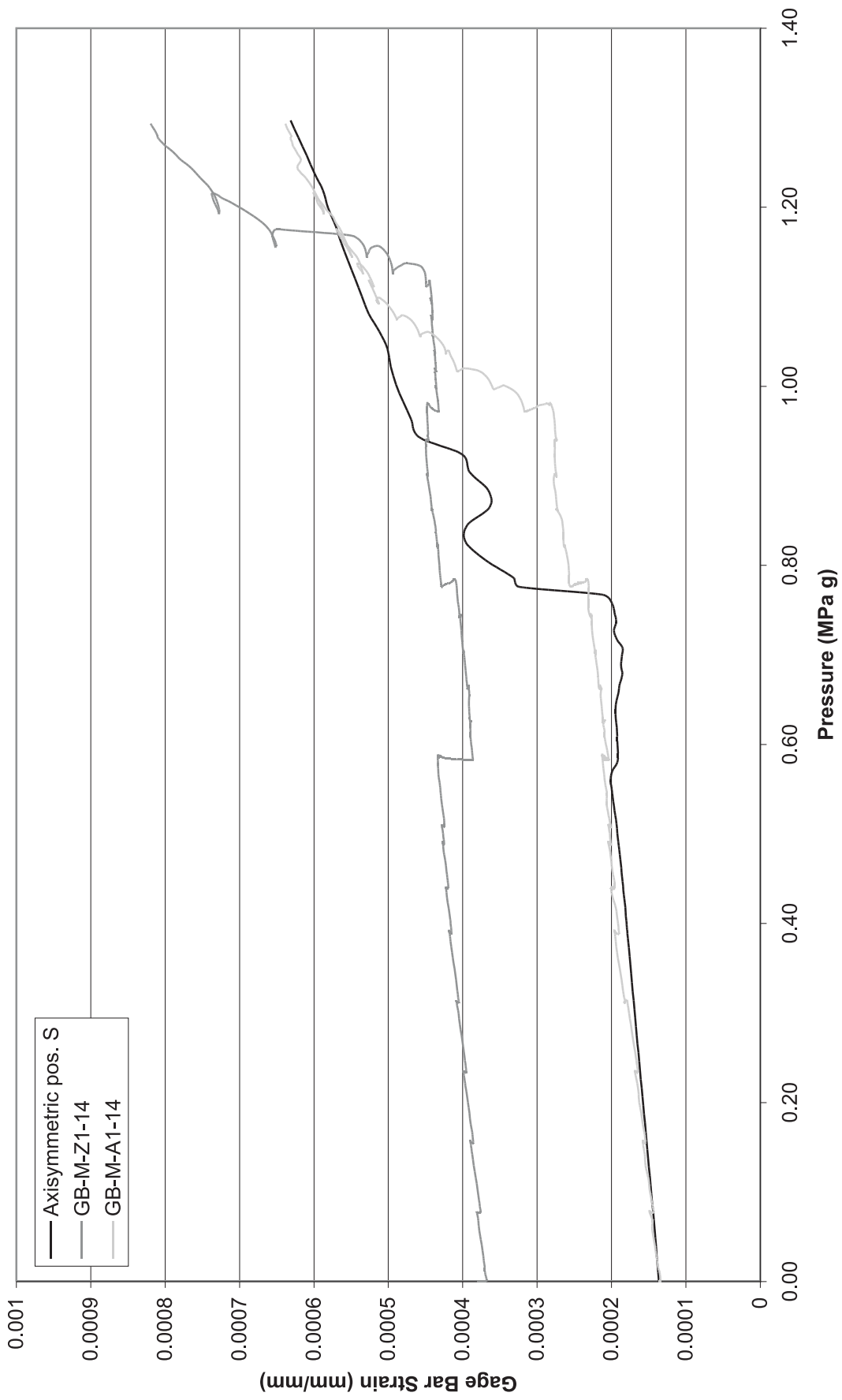


Figure 5-38. Final Posttest Analysis Vs. LST at Wall Base Gage Bar Position S

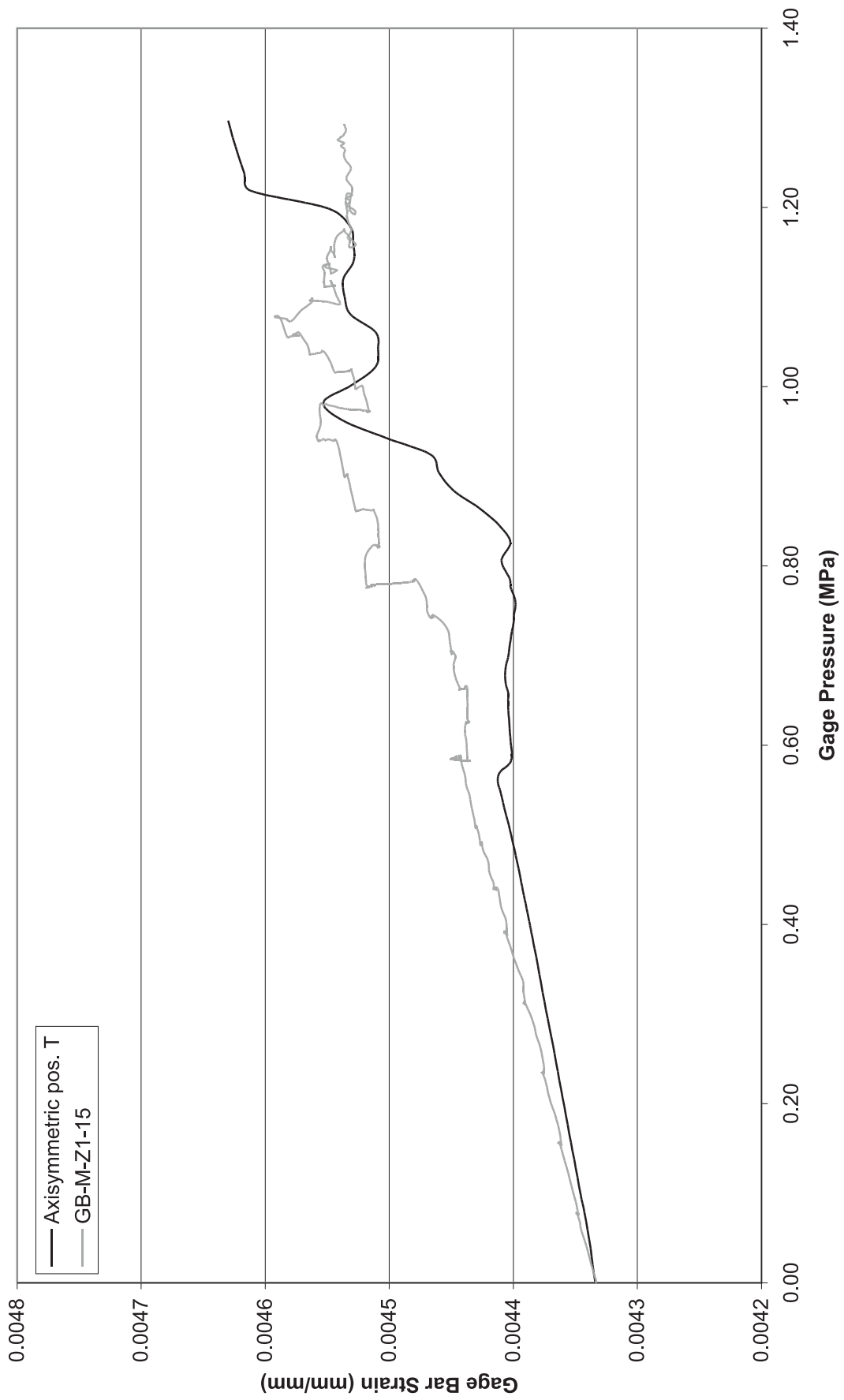


Figure 5-39. Final Posttest Analysis Vs. LST at Wall Base Gage Bar Position T

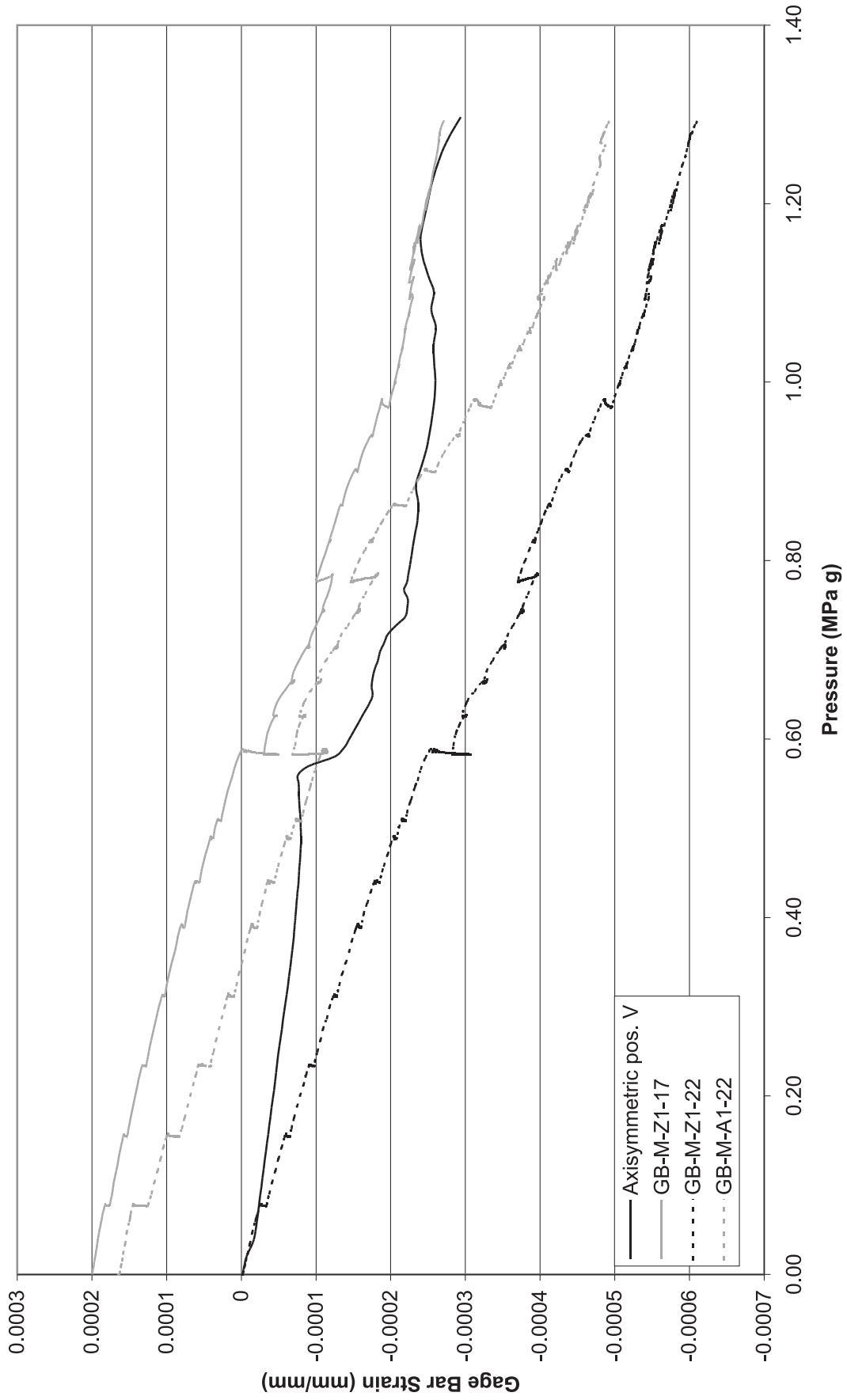


Figure 5-40. Final Posttest Analysis Vs. LST at Wall Base Gage Bar Position V

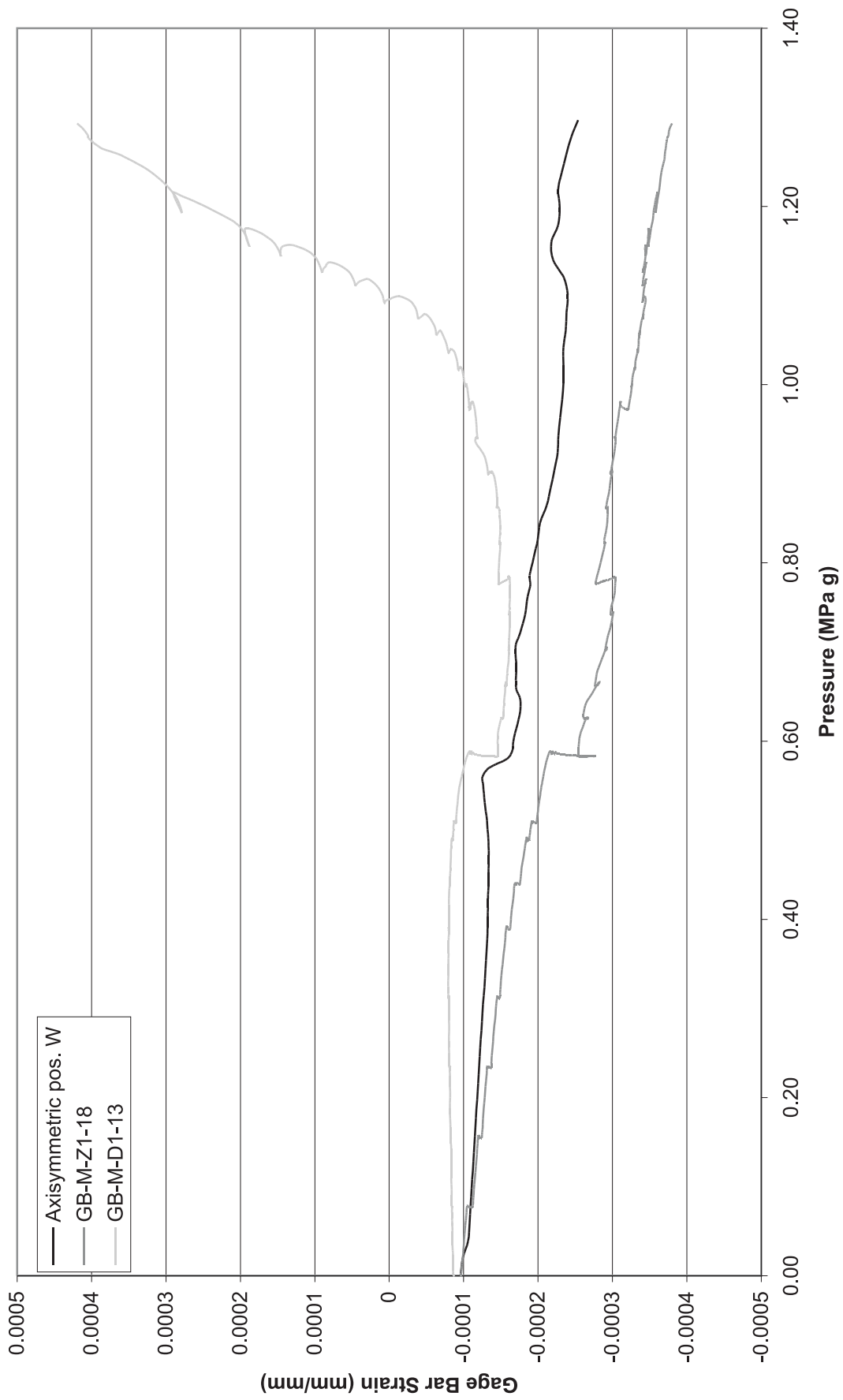


Figure 5-41. Final Posttest Analysis Vs. LST at Wall Base Gage Bar Position W

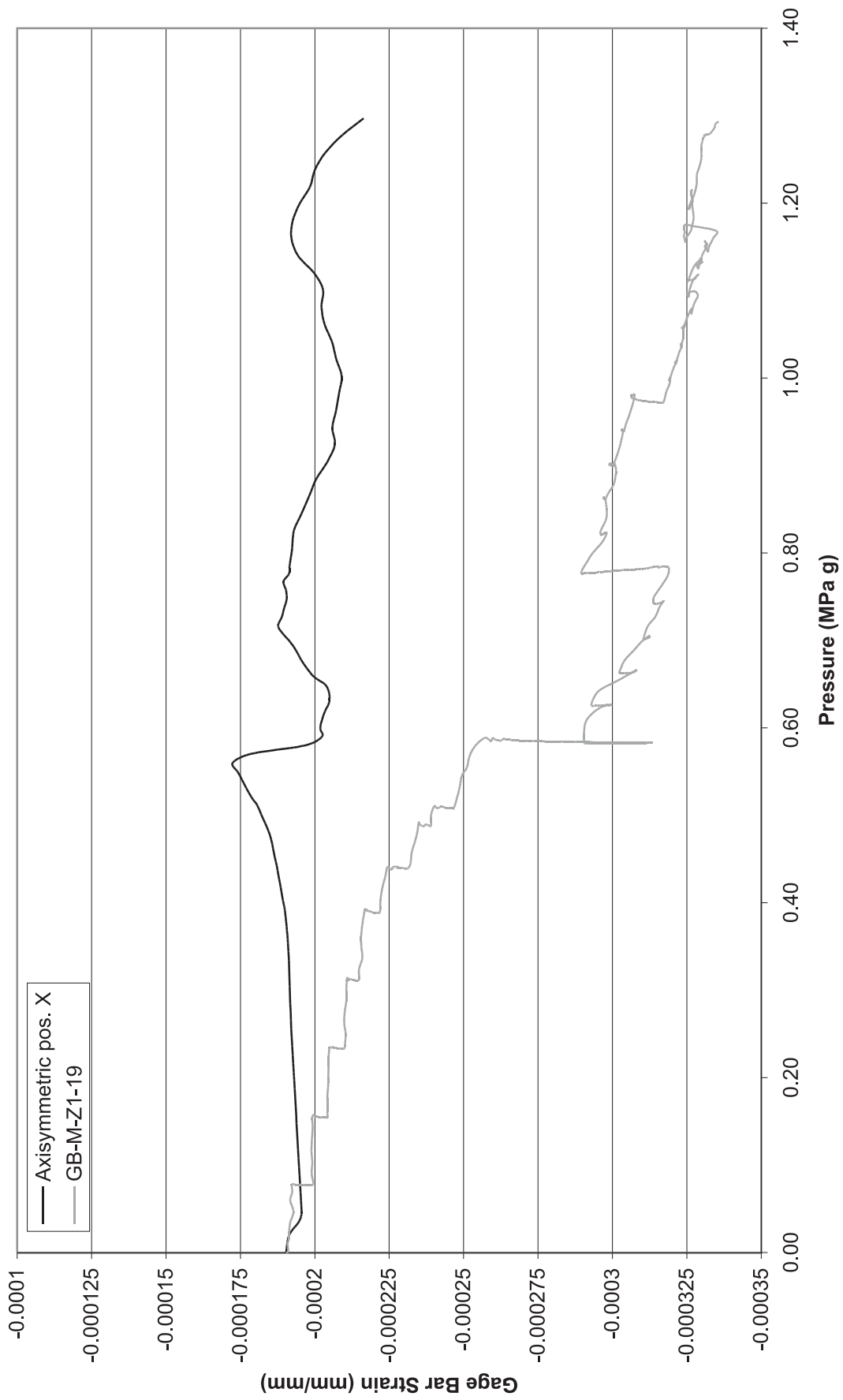


Figure 5-42. Final Posttest Analysis Vs. LST at Wall Base Gage Bar Position X

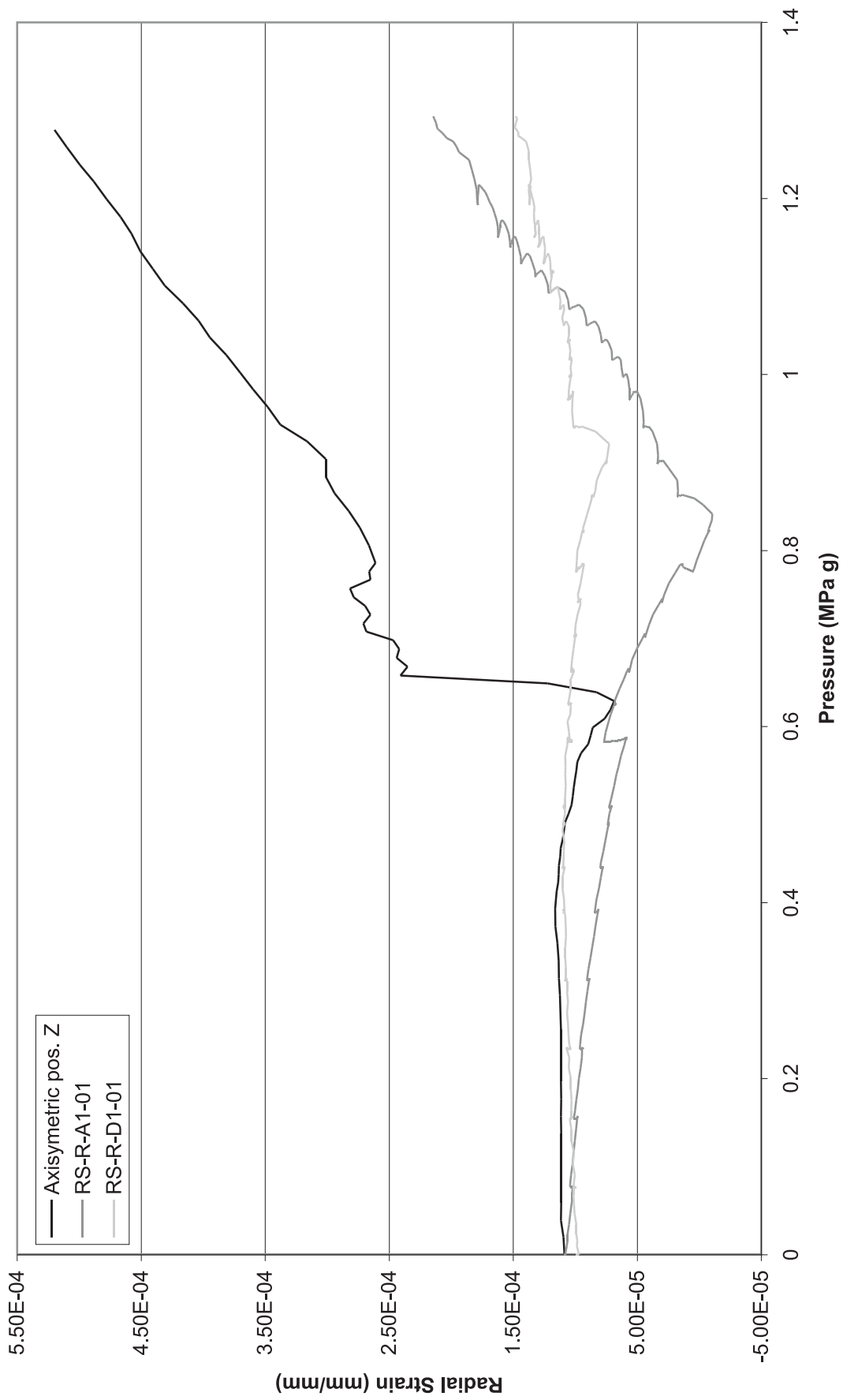


Figure 5-43. Final Posttest Analysis Vs. LST at Wall Base Radial Stirrup Position Z

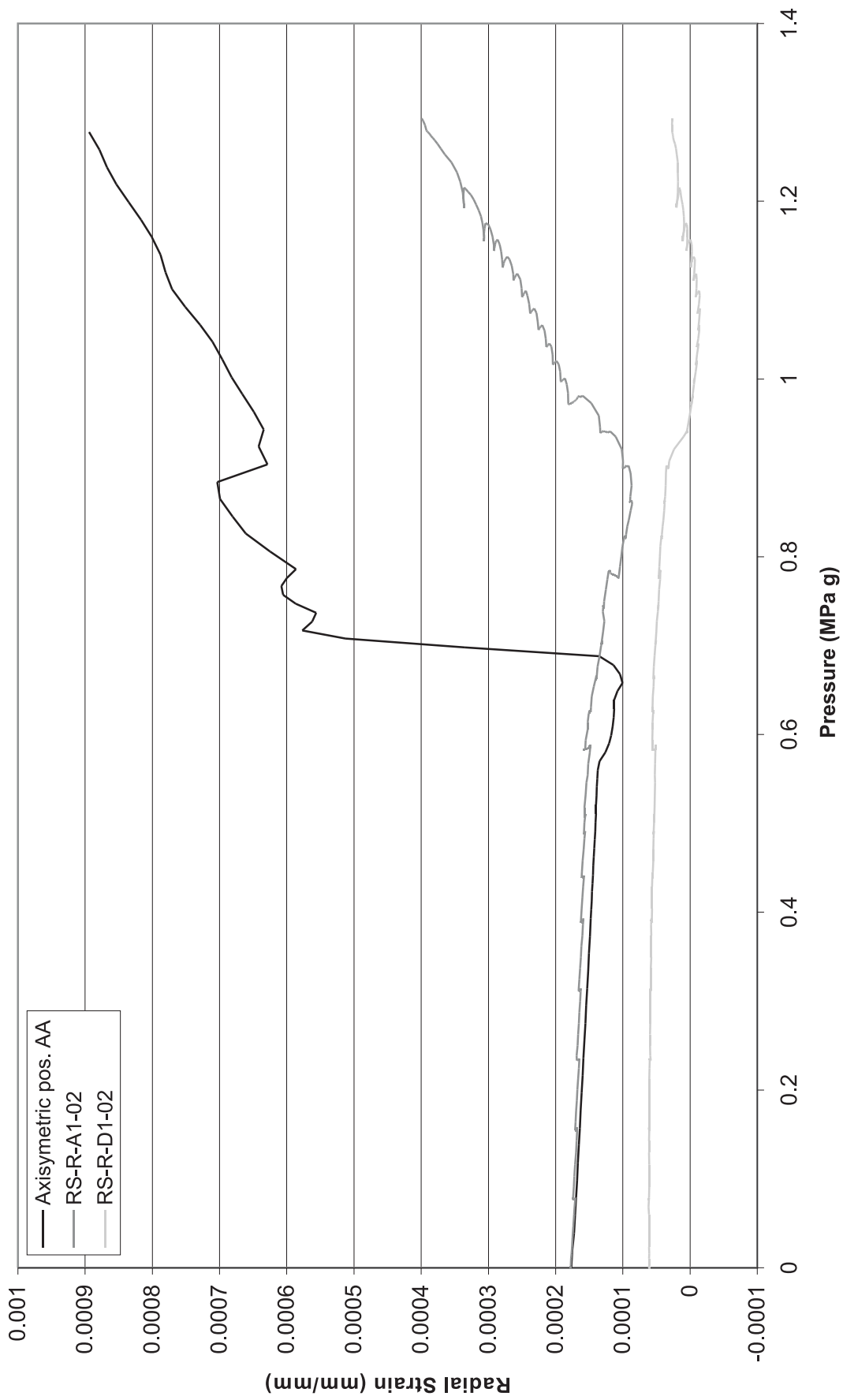


Figure 5-44. Final Posttest Analysis Vs. LST at Wall Base Radial Stirrup Position AA

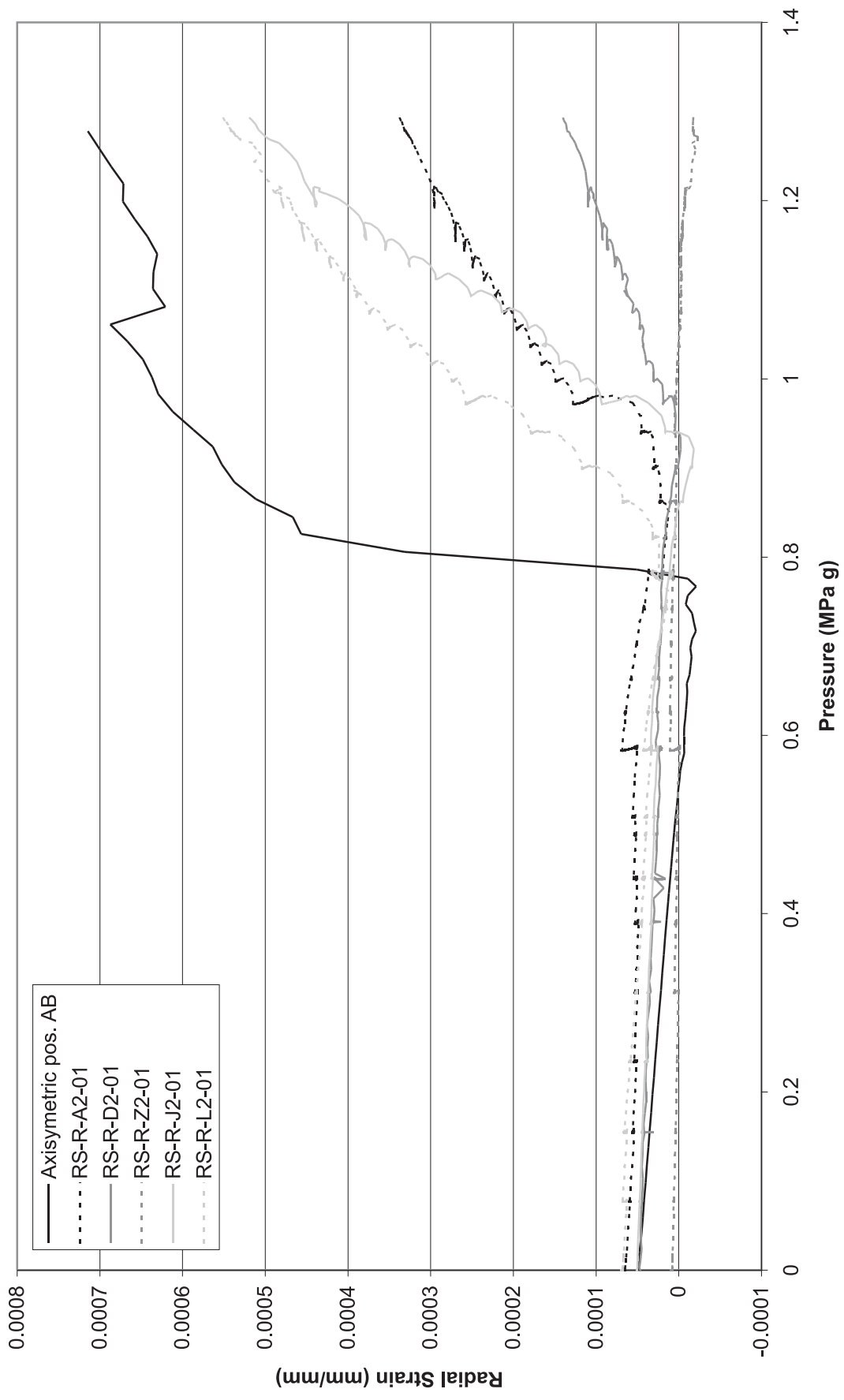


Figure 5-45. Final Posttest Analysis Vs. LST at Wall Base Radial Stirrup Position AB

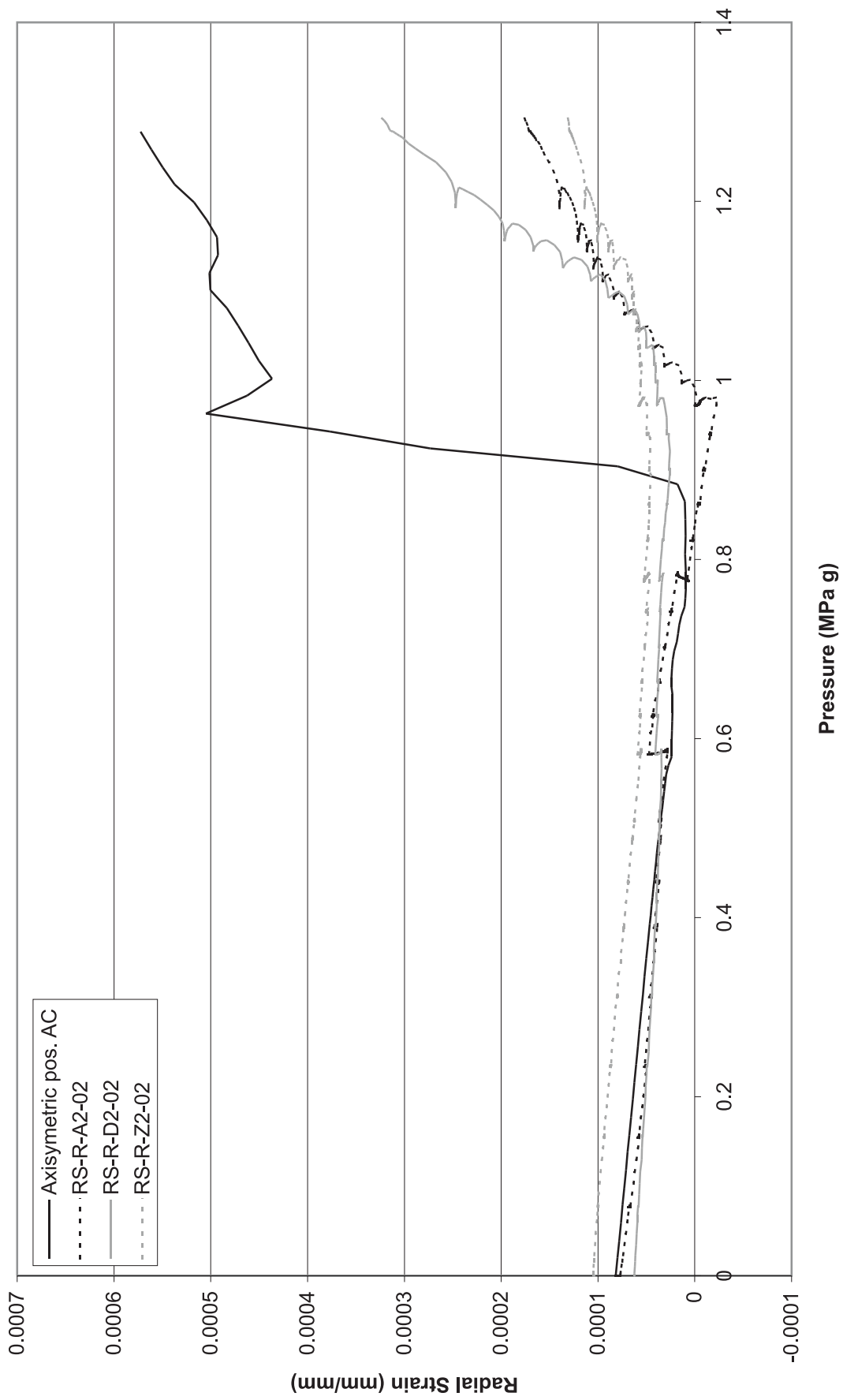


Figure 5-46. Final Posttest Analysis Vs. LST at Wall Base Radial Stirrup Position AC